Alternative seed particles for GaAs nanowire growth

Hallberg, Robert

2016

Document Version:
Publisher's PDF, also known as Version of record

[Link to publication](#)

Citation for published version (APA):
Hallberg, R. (2016). *Alternative seed particles for GaAs nanowire growth.*

Total number of authors:
1

Alternative seed particles for GaAs nanowire growth

Alternative seed particles for GaAs nanowire growth

by Robert Hallberg

LUND
UNIVERSITY

Alternative seed particles for GaAs nanowire growth

by Robert Hallberg

LUND
UNIVERSITY

Faculty of Physics, Solid State Physics

Dedicated to my loved ones
Matilda - Yvonne - Tommy - Christofer

Contents

7   Concluding remarks and outlook

References

Scientific publications

List of publications

This thesis is based on the following publications, referred to by their Roman numerals:

I   **Hydrogen assisted compaction of spark discharge generated nanoparticles**

R. T. Hallberg, L. Ludvigsson, B. O. Meuller, K. A. Dick, M. E. Messing
Manuscript draft (2016)

II   **Palladium seeded GaAs nanowires**

R. T. Hallberg, S. Lehmann, M. E. Messing, K. A. Dick
Journal of Materials Research, **31**(2), p. 176-185 (2016)

All papers are reproduced with permission of their respective publishers.

Acknowledgements

First I want to thank my excellent supervisors and mentors. You are always there when I am confused, and most of the times I am less confused after our meetings. Your support is always very appreciated and you should know that you are doing a great job so far!

Secondly I want to thank all my great present and former co-workers at Solid State Physics and Chemistry Centrum. We are a large group of people and together we create a good work environment.

Thanks to all my friends and acquaintances outside academia, who reminds me that the world is larger than nano.

Special thanks goes to my parents, ny brother and my fiancé. Thank you for encouraging me to do my best and to always value my own happiness! What is life without your sunshine.

Alternative seed particles for GaAs nanowire growth

*It's easy to be complicated
but very difficult to be simple.*
— Debasish Mridha

Chapter 1

Introduction

Today's electronic device technology is largely based upon the miniturization of silicon transistors. To further increase the performance, it is necessary to improve nanostructure fabrication and to extend to other semiconductor materials. One interesting solution is to grow semiconductor nanowires with the aid of a seed particle. A seed particle is a nanoparticle ($5 - 500$ nm in diameter) that selectively promotes growth of a crystalline semiconductor, forming a nanowire structure beneath. Depending on what elements the particle is supplied with, different semiconductors can be grown. The choice of semiconductor is adapted per application, however the metal seed particle is almost always gold [1].

Gold has been found to be an excellent catalyst for growing nanowires, and often outperforms other metals for fabrication of oriented and size selected nanowires [2]. However, gold is also the most studied material, and by extending to alternative materials new possibilities emerge. For example, alternative seed particle materials have been shown to provide: better nucleation of GaSb nanowires [3], prone to nanowire growth in non-$\langle 1\,1\,1 \rangle$B growth directions [4, 5, 6, 7], nanowires with rare crystal structures [8] and to beneficially incorporate as a dopant [9]. This is an advantage compared to gold, which may unintentionally incorporate into Si [10, 11, 12] and other semiconductors [13], where it may deteriorate the electronic properties [14, 15] of the semiconductor device. Hence, research on alternative seed particles will provide an extra degree of freedom when designing nanowire devices and studying the mechanism surrounding particle-assisted growth.

The focus of this work is the development of alternative seed particles and how the nanowire properties are affected by the particle properties. The most commonly used methods for generating seed particles are by: annealing of thin films, dispersion of colloidal solutions [16] and lithography methods that provides excellent size and position control. However, these processes often involve chemical processes that may contaminate the seed particle, substrate

surface and even the fabricated nanowire. In this work a less conventional method is used, where aerosol nanoparticles are generated by a spark discharge generator (SDG), known to produce pristine particles with a high particle size control [17]. The SDG generates aerosol particles by electric ablation between two electrodes, forming agglomerated nanoparticles. The agglomerates are thermally compacted in a tube furnace and deposited with a controlled size and particle density on substrates. The nanoparticle decorated substrates are inserted in a metal-organic vapor-phase epitaxy (MOVPE) machine, where nanowires are grown from the seed particles. By varying growth parameters such as growth temperature and the supply of material, the nanowire properties are affected. The effects are mainly characterised by electron microscopy, namely scanning electron microscopy (SEM) and transmission electron microscopy (TEM).

The results presented in the thesis are separated into two parts, first the development of aerosol nanoparticles, and second the growth of nanowires from mentioned particles. The development of nanoparticles treats a compaction study, where Au, Pd and Co nanoparticles are compacted thermally at different temperatures. Furthermore, we present how hydrogen present at particle generation may effect the compaction. Gallium arsenide (GaAs) nanowires grown from Pd nanoparticles are presented. The focus is on how growth settings can affect nanowire morphology and a discussion around the particle phase.

1   Thesis outline

The thesis is based on two papers, Paper I - Hydrogen assisted compaction of spark discharge generated nanoparticles[1] and Paper II - Pd seeded GaAs nanowires[2]

Chapter 2   Aerosols are airborne particles and in order to generate, reshape, measure and deposit particles of various elemental composition and size, a series of instruments is required.

Chapter 3   With electron microscopy it is possible to resolve nanoparticles and nanowires. Depending on the sample and instrument different signals and imaging modes are used, resulting in different sample information.

Chapter 4   Nanowires are highly symmetric structures due to their crystal structure. They are grown layer-by-layer with epitaxy and are guided by a particle. The particle/substrate interface acts as a preferred precipitation site for dissolved material.

---

[1]Manuscript draft
[2]Published work

Chapter 5   Nanoparticles are compacted thermally, and the aerosol carrier gas composition can affect the compaction behaviour, (paper I).

Chapter 6   Palladium nanoparticles have been used to grow gallium arsenide (GaAs) nanowires. The concept of growth parameters is introduced and paper II is summarised.

Chapter 7   The current particle development is summarised and upcoming hurdles are treated. Particles are used in nanowire growth, and future plans are centred around the role of the particle phase.

Chapter 2

Aerosol production

A spark discharge generator (SDG) is used to produce aerosol nanoparticles for nanowire growth. The SDG uses an electrical discharge between electrodes to locally evaporate material, forming a supersaturated vapor that rapidly condenses into nanoparticles. The path from an initial vapor cloud to deposited nanoparticles is a journey involving interesting physics and instruments that are covered in this chapter. First comes an overview of the aerosol generation and characterization set-up used in this work, followed by a more detailed description of the parts of the system.

1   Instrumental set-up

The set-up (figure 2.1) consists of: a SDG, a ^{63}Ni radioactive charge neutralizer, two tandem differential mobility analyzers (DMAs), a tube furnace, an electrometer and an electrostatic precipitator (ESP). The gas handling is handled with seven mass-flow controllers (MFCs): two for the input of carrier gas, four for the sheath flow of the two DMAs, and one for the system exhaust. The exhaust consists of a particle filter and a rotary pump, used to control the pressure of the system. The system is a medium vacuum system capable of reaching < 10 mbar but is typically operated at atmospheric pressure.

2   Mass flow controller

A MFC is a device used to measure and control the flow of a gas (or liquid). A thermal MFC divides the gas into two laminar flows, with the smaller flow guided through a capillary sensor device. The sensor is equipped with two thermometers used to measure an increase
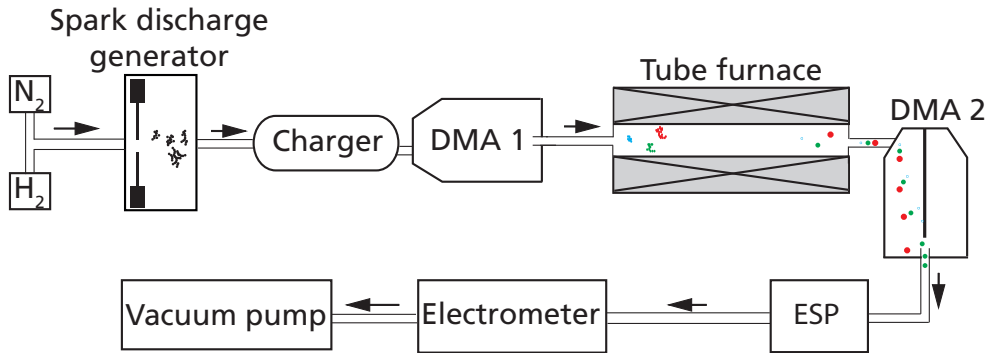
Figure 2.1: The carrier gas of the aerosol system is controlled by two mass flow controllers (MFCs), connected to different gas sources (e.g. N_2, H_2). Aerosol particles are generated in a spark discharge generator (SDG), forming agglomerate nanoparticles transported by the carrier gas. A charge neutraliser enables size-sorting with two differential mobility analyzers (DMAs), separated by a sintering furnace, used for reshaping of nanoparticles by thermal compaction. Finally, an electrometer is used to measure the particle concentration and an electrostatic precipitator (ESP) to deposit particles.

in gas temperature after heating. The temperature difference ΔT is proportional to the heat capacity per mole at constant pressure c_p, the flow Q and a proportionality constant B [18, p.312-315].

$$\Delta T = Bc_pQ$$

For a calibrated MFC, B and c_p are known for the specific gas composition, and the flow can be adjusted by changing a pressure valve. The pressure valve maintains a pressure gradient over the MFC, throttling the flow. The total flow range is limited for an MFC, and they are specified to function in a specific range, e.g. $0-5$ sccm or $0-200$ sccm. However, they are most accurate within the range of $10-90\%$ of their maximum flow [18, p.312-315].

3 Spark discharge generator

Spark discharges have been used since 1988 to produce aerosols of monodisperse gold and carbon nanoparticles [19]. Since then, the technology has matured [20] and found its way into several fields, including, medicine and health, environmental science, and materials science [17]. The number of different materials produced has expanded greatly, and covers a wide variety of metals [19], alloys [21, 22, 23], semiconductors [24], and metal oxides [25].

The SDG consists of two components: a chamber housing the electrodes and an electrical circuit to provide energy for spark discharge between the electrodes.

3.1 Electrical circuit

The electrical circuit, consists of a power source, a capacitor and two electrodes acting as a high voltage switch, see figure 2.2. The power supply charges the capacitor with a capacitance C, gradually increasing the bias V over the electrodes. Eventually V exceeds the breakdown voltage V_B, and an electrical discharge occurs with an energy E proportional to V_b^2. Furthermore, the energy is proportional to the mass of evaporated material and will affect the formed particle distribution [19, 26].

$$E = 0.5CV_b^2$$

To produce a stable concentration of particles it is important that V_b and the supplied current to the capacitor are kept constant, otherwise the frequency and energy of the sparks will vary. According to Paschen's law, V_b is also affected by the electrode distance, the gas composition and the pressure [27, p. 333-339]. Therefore, the electrode distance has to be adjusted as material is evaporated over time [28].
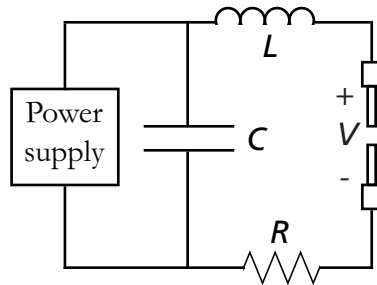
Figure 2.2: An RLC circuit makes up the electrical system of the SDG. A power supply charges a capacitor C that builds up a voltage V over the electrodes. Inductance L and resistance R of the cables makes the circuit non-ideal.

A new, more advanced set-up [29] (not used in this work) avoids variations in spark energy by not relying on the breakdown voltage to trigger the discharge. Instead there is a continuous glow-discharge between the electrodes, and high voltage switches are used to deliver sparks of controllable energy and frequency. Furthermore, this increases the energy efficiency and the maximum spark frequency [20].

3.2 Spark discharge

The SDG chamber consists of two electrodes, separated by a controllable gap distance in the millimetre range. A carrier gas flows between the two electrodes and transports the vapor and formed aerosol particles away from the electrodes, see figure 2.3.
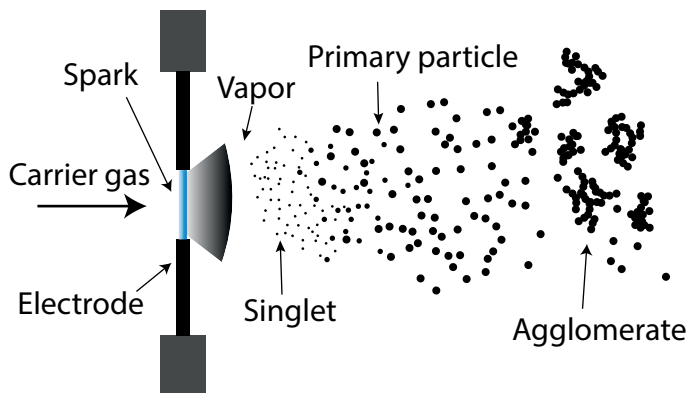
Figure 2.3: During a spark discharge event, material is evaporated, forming a vapor that is quenched rapidly in the carrier gas and forms singlets. Singlets grow by coalescence into spherical primary particles, which are too big to coalesce, and instead form agglomerates.

During a spark discharge event, a plasma channel forms between the two electrodes, which locally superheats and evaporates material at temperatures above 20 000 K [30]. The evaporated material is cooled rapidly, forming a highly supersaturated vapor [30, 31]. As a result, homogeneous nucleation of atomic clusters referred to as singlets occurs. Due to the small size of singlets they grow by coalescence, merging into larger spherical particles [32]. After reaching a critical size the particles do not fully coalesce, and further growth occurs by agglomeration [33]. This forms highly fractal agglomerate nanoparticles, consisting of smaller primary particles. Two primary particles only partially merge, forming a joint volume referred to as a necking region, which grows faster for particles with clean surfaces [34].

4   Size control

To produce spherical nanoparticles of a controlled size it is necessary to compact (see section 5 and chapter 5) the agglomerated nanoparticles and to size-select the nanoparticles in the aerosol phase. Size selection is done by classifying particles according to their electrical mobility diameter, and compaction is done by sintering the particles in a tube furnace.

4.1   Electrical mobility

The particles are non-uniformly charged during generation, and therefore a ^{63}Ni radioactive foil is used to generate bipolar ions that redistributes the aerosol particle charges by collisions, eventually forming particles with a near Gaussian distribution of charges [35]. The smaller nanoparticles are more difficult to charge due to their smaller cross-sectional

area. For particles in the range of $20 - 100$ nm, a majority of the particles are either singly charged or uncharged ($\sim 100 - 80$ %), whereas multiply charged particles are in a minority ($\sim 0.03 - 10$ %) [36]. A singly charged spherical particle of diameter d, can be described according to its electrical mobility Z, according to Stokes' law [37].

$$Z = \frac{neC_c}{3\pi\mu}\frac{1}{d}$$

Where ne is the particle charge, C_c the Cunningham slip correction factor and μ the gas viscosity. For singly charged spherical particles, the mobility diameter is equal to the geometric diameter. However, for non-spherical nanoparticles the two will differ, depending on the particle shape and orientation in relation to the electric field. Therefore, an agglomerate nanoparticle of fixed volume will have a different mobility diameter depending on shape, where the smallest mobility diameter typically corresponds to the most compact shape. An exception is elongated particles, where the mobility diameter strongly depend on particle orientation.

4.2 Differential mobility analyzer

A differential mobility analyzer (DMA) is a common instrument in aerosol physics to size-select aerosols by their electrical mobility. A DMA consists of a grounded cylinder with a central rod, separated by a sheath gas flow, aligned parallel to the cylinder. The rod is biased with respect to the cylinder wall, forming an electric field perpendicular to the sheath flow. The particles travel with the sheath flow and are displaced by the electric field. Depending on their electrical mobility diameter, the particles are either: collected by the rod or cylinder wall, or exit through a slit or sheath flow. By first using the charge neutralizer, mainly singly charged particles enter the DMA, and only particles of the selected size and polarity can exit through the slit. An increase in electric field strength results in larger particles exiting the slit, and by inverting the applied bias between the central rod and the cylinder wall, also the selected particle polarity is inverted.

5 Thermal compaction

For nanoparticle applications highly uniform and well characterized nanoparticles are often preferred. To achieve this it is necessary to compact agglomerates into well-defined spherical nanoparticles, where the size and material properties can be measured and used to predict the particle properties. One common method of compaction is to sinter the particles,

subjecting them to a high temperature that increases the rate of solid diffusion. With an increase in diffusion, matter can rearrange and form more energetically favorable structures or phases. Diffusion can in turn be divided into bulk, grain boundary and surface diffusion, whereof surface diffusion is typically the fastest [38]. Furthermore, the small size and low fractal dimensions of agglomerates further promote surface effects.

The compaction of agglomerate nanoparticles is driven by a minimisation of surface energies. It has been proposed that this occurs by either a reconstruction of primary particles or by coalescence of primary particles [34]. During reconstruction, the primary particle size is the same but the total surface area can be minimized by clustering, forming a more condensed particle [34]. Coalescence on the other hand, decreases the total surface area by merging primary particles, forming fewer larger primary particles [39].

During thermal compaction of aerosol nanoparticles, three steps can typically be identified from the sintering curves (see chapter 5 figure 5.1): compaction, internal rearrangement and finally evaporation [40]. At low temperatures the material compacts with increasing temperature. At $30 - 60$ % of the bulk melting point (in Kelvin) a maximum compaction is typically reached, i.e. where no more decrease in diameter occurs, after which only internal rearrangement occurs. During this rearrangement the crystal structure changes and new facets may form [34, 41], sometimes without actual melting occuring. At very high temperatures, evaporation can be significant as the vapor pressure increases with temperature.

By reaching a spherical shape the surface to volume ratio is minimized, resulting in a reduction of total energy. If different facets have very dissimilar surface energies, the corresponding facet areas will also be dissimilar, resulting in an anisotropic particle, as described by the Wullff's theorem.

$$\Delta G_i = \sum_{j=1} \gamma_j O_j$$

To minimize the Gibbs free energy ΔG_i the sum of the product of surface energies γ_j and their respective surface area O_j should be minimized. This effect mainly occurs at high sintering temperatures, when the particle is already fully compacted and the total surface area is close to minimized.

6 Electrometer

An electrometer is used to measure the particle concentration at the outlet of the system. To measure the concentration it collects the nanoparticles and a current is generated as a

result of the particle charge. Assuming the particles are singly charged and the gas flow is known, the sensitivity of the TSI aerosol electrometer 3068B used corresponds to $\pm$ 6250 particles per second. Therefore, an electrometer is an excellent method of measuring the particle concentration for the SDG, which generates $10^6 - 10^9$ size-selected particles per second.

7   Electrostatic precipitator

The electrostatic precipitator (ESP) is used to collect particles on a substrate. This is done by placing the substrate on a metal plate, which collects the nanoparticles with an applied bias of $2 - 10$ kV. Particles enter the ESP from above and perpendicular to the substrate. As the particles travel across the substrate they are collected by the electric field uniformly within a deposition spot. Small particles have a higher electrical mobility, hence they are deposited in a smaller spot than large particles. By decreasing the applied bias or increasing the distance between the metal plate and the ESP inlet, the spot-size diameter can be increased. Finally, the deposited particle density is estimated from the carrier gas flow, particle concentration, spot-size and deposition time.

Chapter 3

Electron microscopy

An electron microscope uses a beam of electrons that by interacting with a sample generates detectable and interpretable signals. In this work, scanning electron microscopy (SEM) was used to image the morphology of nanoparticles and nanowires on semiconductor substrates, and transmission electron microscopy (TEM) to determine the crystal structure, morphology and composition of nanoparticles and nanowires. This chapter covers why electrons provide a good source for illumination, how the sample is illuminated and the different imaging techniques used in this work.

1 Resolution

Electron microscopes were first developed to bypass the fundamental resolution limit of conventional visible-light microscopy, which is the Rayleigh criterion. The Rayleigh criterion states that due to diffraction the smallest resolvable distance d between two objects is inversely proportional to the wavelength. For a typical conventional visible light microscope this limits the resolution to roughly half the wavelength $\lambda_{blue}/2 \approx 200$ nm, whereas it for an electron microscope limits the resolution first at the picometer scale. This comes from the small de-Broglie wavelength λ of a high energy eV electron with the effective mass m_0.

$$\lambda = \frac{h}{\sqrt{2m_0 eV(1 + eV/2m_0 c^2)}}$$

However, due to other limiting factors an electron microscope does not reach the diffraction

limit. In a transmission electron microscope (TEM) the resolution is limited by aberrations of the electromagnetic lenses used to focus the electron beam. For a scanning electron microscope (SEM) the resolution is limited by the spread of the electron beam inside the sample, elaborated upon in section 3.

2   Illumination system

A field emission gun (FEG) (figure 3.1) is an electron source with a very sharp tip that is biased with respect to a primary anode, responsible for extracting electrons. A secondary anode, or a series of secondary anodes further accelerates the electrons with an acceleration voltage V, resulting in electrons with the energy eV. Together, the anodes function as an electrostatic lens, focusing the electrons into a crossover, acting as a virtual light-source. [42, p.73-81]. In this work two different FEG equipped microscopes have been used, a 15 keV Hitachi SU8000 SEM and a 300 keV JEOL 3000F TEM.
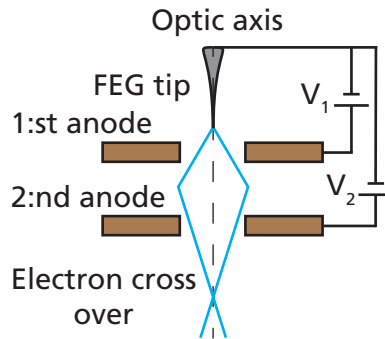
Figure 3.1: Schematics of a field emission gun (FEG). The first anode extracts electrons from the sharp tip with a bias V_1, which are accelerated by the secondary anode(s) with the bias V_2. The combined field of the anodes forms a fine crossover of electrons.

The incident beam that interacts with the sample is operated in one of two modes. Either the beam is broad, nearly parallel and illuminates a larger area of the sample, or the beam is narrow, converged and has to be scanned across the sample. Switching between the two modes is done by focusing the electron beam with a series of condenser lenses, situated between the electron gun and the sample.

3 Detectable signals

An incident electron that interacts with a sample results in several detectable signals, see figure 3.2. Some of the signals, such as backscattered electrons and cathodoluminesence are not essential for this work and are excluded from further discussion. However, signals marked in bold are described below. For a thin sample as in figure 3.2 the beam is transmitted through the sample and the emitted signals are localised to the illuminated area. However, for very thick samples used in for example SEM, the beam widens as it enters the sample. This results in that the signals originate from a larger volume referred to as the excitation volume, and often limits the spatial resolution of the specific signal type.
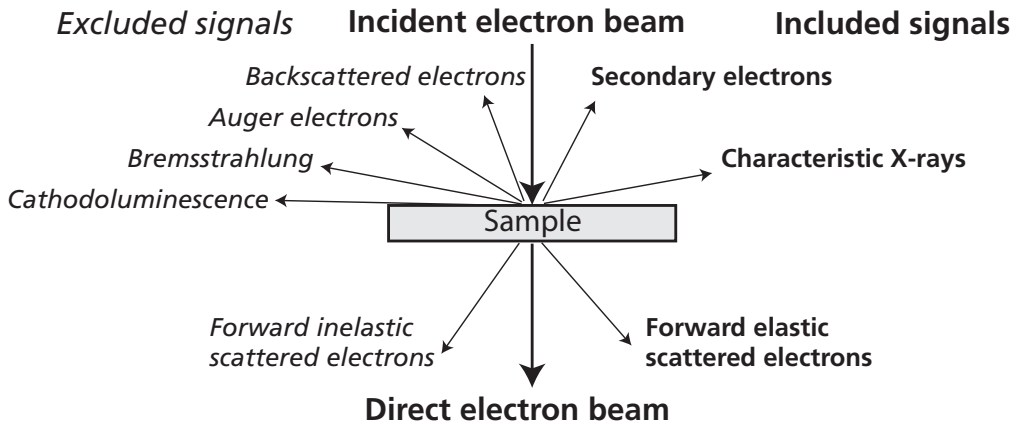
Figure 3.2: Schematics of the different signals generated when a high energy electron beam interacts with a thin sample

Secondary electrons are low energy electrons (< 50 eV) generated from primary radiation, i.e. the incident or scattered electron beam, that interacts with the sample. Due to the low energy of secondary electrons they can only penetrate a few nanometers in bulk materials and contribute to a high resolution signal. The low escape depth results in that only secondary electrons generated in a close-proximity to a surface are emitted, and can reach the detector. The secondary electrons are detected by a positively biased secondary electron detector, that effectively attracts and collects secondary electrons. The detector can also be used as a complementary signal in scanning transmission electron microscopy (STEM), to provide topological information.

Characteristic x-rays originate from transitions between different electronic energy levels of an atom. Transitions occur after an inner electron has been ejected by the incident beam. As the electronic structure differs between elements the emission spectrum is elemental specific and can be used to identify and quantify elements in a SEM or TEM equipped with an energy dispersive x-ray (EDX) detector. The detector is coupled to spectral analysis

software that: identifies elements, deconvolve overlapping peaks and quantifies elements. Elements are identified by comparing the detected spectra to the expected spectrum for different elements. The relative positions and intensities of different electronic transitions are known, and therefore it is possible to deconvolve overlapping peaks and to quantify the composition.

The incident electron beam is almost fully transmitted through the very thin TEM sample ($<$ 100 nm) and a majority of the electrons are unaffected (direct beam) or scatter elastically with the sample. For low scattering angles ($< \sim 10°$) the scattered electrons are usually coherent with the direct beam. Electrons that have lost energy are referred to as inelastic scattered electrons and typically scatter incoherently at low angles ($< 1°$).

4 Imaging modes

The imaging modes used in this work include high resolution TEM, (selective area) diffraction and SEM.

4.1 High resolution TEM

High resolution TEM mode is operated with a broad and parallel beam. Due to the wave properties of electrons, an objective lens situated beneath the sample can form an image and/or diffraction pattern of the illuminated area. The contrast in a high resolution TEM image is primarily made up from phase-contrast.

When electrons propagate through matter, their phase in relation to electrons propagating through vacuum shifts. For an image consisting of primarily coherent electrons, the phase shift will contribute to an interpretable contrast. However, this is only true if the phase shift is small, which is true for thin structures within the resolution limit of the microscope.

4.2 Selective area diffraction

A requirement for high resolution imaging and diffraction pattern imaging is a crystalline sample that is tilted along a zone axis (crystallographic orientation). A crystal oriented along a zone axis will have atomic planes ordered perpendicular to the incident beam direction. The Bragg condition is fulfilled for the aligned set of planes hkl, where h, k and l are Miller indices that describes the orthogonal direction of the plane. Therefore, constructive interference occurs when the product $2d_{hkl}\sin(\theta)$ equals an integer number of electron wavelengths, $n\lambda$, where θ is the angle between the incident beam (or exit beam) and reflection plane.

$$n\lambda = 2d_{hkl}\sin(\theta)$$

An aperture is used to limit from where on the sample the diffraction pattern is created. When using such an aperture, a selective-area diffraction pattern (SADP) is acquired.

The reciprocal lattice of a crystal is imaged when viewing the diffraction pattern or the fast-fourier transform (FFT) of a high resolution image. Each spot in the reciprocal lattice corresponds to a set of planes that fulfils the Bragg condition. In reciprocal space, a distance r between spots corresponds to a repeating pattern with the frequency $1/r$. The angle between two reflection spots, ϕ is equal to the angle between two set of crystal planes, and be used to describe and determine directions in reciprocal space. By comparing the angles and relative distances between spots to literature, the crystal structure can be determined.

4.3   Scanning electron microscopy

In scanning electron microscopy (SEM) and scanning transmission electron microscopy (STEM), a small area is illuminated with a focused narrow beam ($\sim 0.1 - 5$ nm). An image of the sample is constructed by scanning the beam across an array of positions and correlating the signal to a pixel in the image. In this thesis, SEM has been used to image the secondary electron emission of the sample, providing topological information. Furthermore, STEM has been used to spatially control the emission of characteristic x-rays, providing elemental composition from controlled areas.

Chapter 4

Nanowires

Nanowires are high-aspect ratio structures with nanometer scale diameters and micrometer scale length. Fabrication of nanowires can be done by two different approaches, top-down or bottom-up. With a top-down approach nanostructures are fabricated by selectively etching a bulk substrate, removing unwanted material. This is a wasteful method that is limited to the material available in bulk form and how anisotropic the etching process is. A bottom-up approach is a less wasteful method, where nanowires are built up layer-by-layer with atomic precision on a suitable substrate. Performed on a crystalline substrate, this is referred to as epitaxial growth, and is this method enables the fabrication of materials with extreme aspect ratios. As the material of a grown structure is not defined by a bulk sample it is a versatile method, capable of fabricating structures of varying compositions and crystal structures - not necessarily available in bulk form.

This chapter first introduces the concept of crystal structure and epitaxy. Therafter, metal organic vapor phase epitaxy (MOVPE) and the role of precursor molecules are presented. Finally particle assisted growth is explained as transport of atoms from precursor molecules to the nanowire/nanoparticle interface. We will focus on a description where growth takes place in a kinetically limited regime and the barrier for nucleation is the lowest at the nanoparticle/nanowire interface.

1   Crystal structure

The definition of a crystalline material is a solid material with a long-range order. By using known symmetries of a crystal structure, it is possible to extrapolate the position of every bulk atom of said crystal.

1.1 Unit cell

The unit cell of a crystal structure is the smallest possible volume that stacked repeatedly forms an infinitely large single crystal. For semiconductors two common crystal structures are cubic zinc blende (ZB) and hexagonal wurtzite (WZ). Zinc blende consists of two interconnected face-centered cubic (fcc) lattices that are displaced relative to each other by $(\frac{1}{4}, \frac{1}{4}, \frac{1}{4})$ unit cell. Similarly, wurtzite consists of two hexagonal close-packed (hcp) lattices, displaced by $(0, 0, 0, \frac{1}{2})$ unit cell.

1.2 Close packed direction

A close packed direction is defined as the direction in which the atomic distances are the smallest. For ZB these are $\langle 1\,1\,1 \rangle$ and for WZ the $\langle 0\,0\,0\,1 \rangle$ directions. In figure 4.1, ZB and WZ are viewed with a close packed direction pointing upwards in the figure.

The bilayer is the smallest repetitive unit, consisting of a monolayer of group III atoms and a monolayer of group V atoms. The first bilayer is denoted A and the second B. However, the third bilayer may either be A or C, depending whether - it is translated in respect to the first bilayer. The periodicity of these layers is referred to as a packing sequence, and is used to discern polytypes of close packed structures. For example, ZB has a ABC stacking and WZ has a AB stacking. Additional polytypes of higher orders includes 4H (ABCB) and 6H (ABCACB), but are increasingly rare.
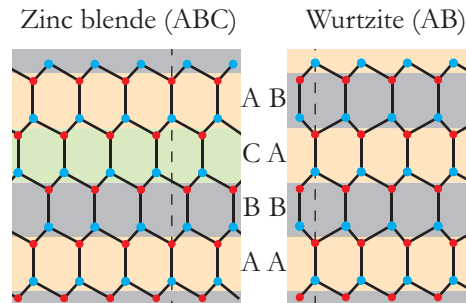

Figure 4.1: Two types of close packing, cubic close packed zinc blende requires three bilayers to form a repetitive unit (ABC). The hexagonal close packed wurtzite requires only two (AB).

2 Epitaxy

Epitaxy comes from the greek words, *epi* (upon) and *taxis* (order), and refers to the growth of a crystalline layer on top of a crystalline substrate. Homoepitaxy is the simplest form of

epitaxy, where both the substrate and crystalline layer are of the same material and crystal structure. Heteroepitaxy combines two different materials and crystal structures, which is more complicated as differences in lattice parameters will create strain at the interface of the two structures. This can in turn result in structural defects, such as dislocations [43].

The supply phase is versatile in epitaxy, and vapor, liquid and solid phase epitaxy are all well developed techniques for growing semiconductor crystals. However, the focus of this work is upon vapor phase epitaxy. Vapor phase epitaxy is divided into physical vapor deposition (PVD) and chemical-vapor deposition (CVD). A prominent technique within PVD is molecular-beam epitaxy (MBE), performed in a high-vacuum atmosphere. Main advantages include; in-situ characterisation and the ability to deposit epitaxial metal films in-situ at cryogenic temperatures [44]. However, it is a slow process in comparison to metal organic vapor-phase epitaxy (MOVPE) used in this work, which is used for industrial applications. MOVPE is an example of a CVD technique where metal organic precursors and hydride sources deposit material that can only be incorporated afer chemical processes that takes place in close proximity to the sample [43].

2.1   Metal organic vapor phase epitaxy (MOVPE)

The MOCVD system used in this thesis work is an AIXTRON 3x2" close coupled shower-head (CCS) MOCVD reactor, see figure 4.2. Hydrogen is used as a carrier gas, supplying metal organic precursors and hydrides to the reactor zone. Furthermore, the metal organic precursor gas lines are equipped with EPISON controllers that further increases the precision of the precursor flows. For purging of the system, high purity nitrogen (99.999 %) is used - required before opening the system for sample exchange.

Inside the reactor, samples are resting upon a heated graphite susceptor, and the precursors are injected separately at a close proximity from the sample. In order to improve the homogeneity of the gas flow the susceptor rotates. The total pressure P_{tot} is set to 100 mbar and the total flow Q_{tot} to 8 slm but is variable.

2.2   Precursors

Two types of precursors are used in MOVPE, metal organic (MO) precursors and hydride sources. The MO sources are stored in bubblers situated in separate temperature controlled water-glycol baths. As the bubbler temperature T is well controlled, so is the equilibrium vapor pressure P_{eqMO} of the precursor. A majority of the sources are liquid resulting in a highly controlled vapor pressure by tuning the temperature and pressure. For trimethyl-gallium (TMG) the vapor pressure of is described by the function plotted in figure 4.3, and is an important property used to control the available material for growth.
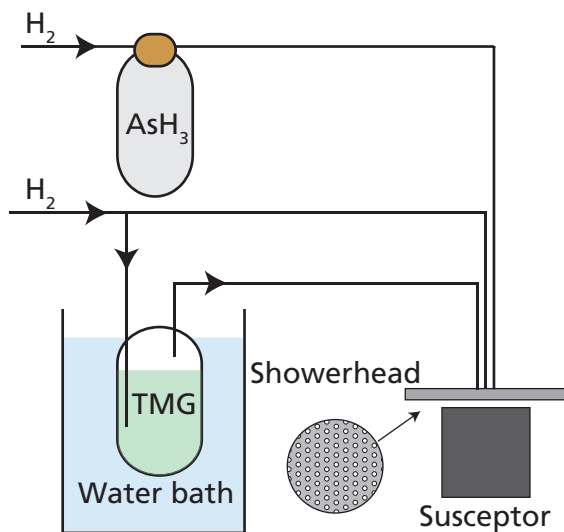
Figure 4.2: Schematics of a CCS MOCVD system: MO sources are situated in bubblers, wheras hydrides are stored in gas bottles. The carrier gas H_2 transports the precursors to the close coupled showerhead (CCS) reactor, and the gases are mixed in close proximity to the samples on the heated susceptor.

$$\frac{P_{MO}}{P_{tot}} = \frac{P_{eqMO}}{P_B} \frac{Q_{MO}}{Q_{tot}}$$

Group V precursors are often hydrides, and are more labile than organic precursors, resulting in a much higher vapor pressure. The vapor pressure is high enough for them to be stored in gas bottles. Therefore, the saturation term $\frac{P_{eqMO}}{P_B}$ is 1 for hydrides and the expression is simplified.

$$\frac{P_{Hyd}}{P_{tot}} = \frac{Q_{Hyd}}{Q_{tot}}$$

3 Precursor decomposition

Decomposition is a type of reaction where a molecule divides into simpler parts; a reaction where bonds are broken as a result of a high energy collision. By increasing the pressure and temperature the molecules in a gas move faster, resulting in an increase of collisions with sufficient kinetic energy to decompose a molecule. Moreover, by reducing the bond energy

Figure 4.3: Vapor pressure of TMG in the interval −20 to 40 °C.

the required kinetic energy is reduced [45, p. 559-563]. This serves as a first approximation to describe why the rate of precursor decomposition increases: with temperature and pressure, by catalytic effects (from surfaces and other molecules) as well as for more labile precursors.

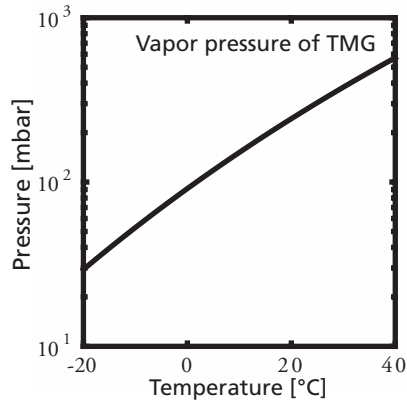The decomposition of TMG and AsH_3 is mainly heterogeneous at lower growth temeperatures. Studies on GaAs growth in MOCVD have shown that TMG and AsH_3 start to decompose at 325 °C and are fully decomposed at 480 °C and 525 °C respectively. However, both precursors fully decompose at temperatures below 450 °C when together [46]. In addition, as chemistry of surfaces may catalyse the decomposition, different facets and materials are believed to further increase decomposition.

MOCVD growth is divided into either kinetic or mass transport limited growth. For kinetically limited growth, the growth rate is limited by thermally activated reaction such as decomposition or nucleation. As the reactions are thermally activated their rate increases with temperature. At higher temperatures, kinetic effects are less important and growth is limited by the diffusion of material (mass-transport). For nanowire growth kinetic effects such as a smaller nucleation barrier at the particle or an increased decomposition in the vicinity of the nanoparticle are responsible for the uni-directional growth. Therefore, during the continuation of this thesis growth will be discussed in a kinetically limited regime.

4 Nanowire growth

A prerequisite for nanowire growth is that the growth rate is highly anisotropic and preferably uni-directional. However, cubic crystal structures are highly symmetric, and multiple equivalent growth directions exist, e.g. the most common growth direction for III-V

nanowires, $\langle 1\,1\,1 \rangle$B, represents four equivalent directions. However, by using a $(1\,1\,1)$B substrate three directions are hindered as they are directed into the substrate, leaving only the vertical $[\bar{1}\,\bar{1}\,\bar{1}]$.

An alternative method known as selective-area epitaxy uses a patterned oxide or nitride mask to inhibit growth everywhere except in its holes [47]. However, we will focus at particle-assisted growth where a seed particle is used to promote growth at the particle/substrate interface.
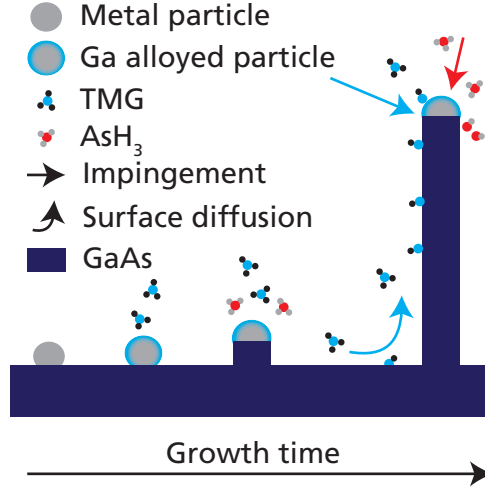
4.1 Particle assisted growth

Using nanoparticles to promote highly anisotropic growth is a well used technique [48], not only for III-V nanowire growth but also employed extensively in other material systems, e.g. Si, Ge [49], ZnO [50], SnO [2] and carbon nanotube growth [51]. In the early days of the nanowire field nanowire growth was proposed to only occur from liquid nanoparticles by a mechanism known as vapor-liquid-solid (VLS) [52, 53]. However, growth has been observed also for solid particles [54, 55], described with a vapor-solid-solid (VSS) mechanism [56]. Another useful mechanism is the preferential interface nucleation (PIN) mechanism [57], which emphasizes the particle's ability to collect material and to reduce the nucleation barrier for growth. These are both properties that are affected by the material phase and are thus parameters in a more general model, able to treat growth with different phases, both for the particle and the supply phase. In this work a vapor supply is used due to the MOVPE method used..

Figure 4.4 depicts particle assisted growth of GaAs nanowires on a GaAs substrate. Decomposed precursors release group III and V adatoms that can diffuse to the seed particle. Often the diffusion length of the group III and V is very different, e.g. TMG has a long diffusion length and incorporates mainly via surface diffusion, whereas AsH_3 has a very short diffusion length and only incorporates by direct impingement. As material is incorporated into the seed particle it becomes supersaturated and nucleation of a bilayer is initiated at the triple-phase-boundary (TPB), a small region where the particle, nanowire and vapor meet.

4.2 Nucleation

Nanowire growth proceeds via a series of nucleation events occurring at the TPB with a nucleation rate k_{nuc}, described according to classical nucleation theory (CNT) to follow a simple Arrhenius expression [58].

Figure 4.4: Schematics of particle-assisted growth of a GaAs nanowire, starting with an initial metal nanoparticle that alloys with Ga. When critically supersaturated, GaAs is precipitated at the nanowire/particle interface, resulting in the growth of a nanowire. The major pathways of gallium and arsenic atoms to be incorporated into the nanowire are illustrated: gallium adatoms diffuse from the substrate, nanowire side facet as well as direct impingement, with direct impingement being the only source for arsenic incorporation

$$k_{nuc} = N_s Z j e^{-\Delta G^*/k_b T}$$

Here, ΔG^* is the change in Gibbs free energy at the critical nucleus size r^*, N_s the number of nucleation sites, j the rate at which molecules attach to the nucleus and Z the Zeldovich factor. The Zeldovich factor is related to the probability of growth with respect to shrinking. More importantly it is evident that a decrease in ΔG^* exponentially increases the nucleation rate k_{nuc}.

To minimize ΔG^* we begin with the expression for Gibbs free energy of forming a new nucleus ΔG. It consists of a supersaturation $\Delta \mu$ related volume term and a surface energy γ related area term.

$$\Delta G = -\Delta \mu \frac{V}{V_{mn}} + \sum_n \gamma_n A_n$$

Here, V is the volume of the formed nucleus, V_{mn} its molar volume and A the area of facet n. As the expression consists of a volume and an area term Gibbs free energy can be minimized as a function of the nucleus radius r, reaching a critical nucleus size r^*. Ignoring

27

shape factors r^* is proportional to $\gamma/\Delta\mu$. Inserting r^* into ΔG yields that also G^* increases with surface energy and decreases with supersaturation.

$$G^* \propto \frac{\gamma^2}{\Delta\mu}$$

In conclusion, an increased growth rate is expected for a small nucleation barrier G^*, and the nucleation barrier is decreased by reducing surface energies γ and increasing the supersaturation $\Delta\mu$ [18, p. 155].

4.3 Chemical potential and surface energy

For a unary system the chemical potential difference between two phases is a measure of the supersaturation (or supercooling) of the system. Assuming the ideal gas law, the supersaturation $\Delta\mu$ is expressed as the partial pressure p of a given phase α from its equilibrium partial pressure p_{eq}.

$$\Delta\mu = RT\ln\frac{p_\alpha}{p_{eq}}$$

The driving force for crystallization is the lowering of chemical potential μ, transitioning from phase α to phase β. Thus for a phase transition to occur the difference between the end state β and beginning state α, the supersaturation $\Delta\mu$ must be negative. For convenience only the absolute magnitude of the supersaturation is used.

$$\Delta\mu \equiv \mu_\beta - \mu_\alpha$$

For nanowire growth to occur with a stable particle size it is necessary that the chemical potential of the vapor phase is higher than or equal to that of both the particle and crystal. Otherwise, material will not be collected by the particle.

$$\mu_{supply} \geq \mu_{particle} \geq \mu_{nanowire}$$

This states that **the nanowire is not supersaturated** with respect to the particle or vapor. A supersaturated nanowire would be absorbed by the particles or evaporate. Interestingly

the supersaturation has to be the highest in the vapor phase, and if excluding the effect of surface energies, nucleation should be the highest in contact with the vapor. Therefore, we can expect the supersaturation to be high in the small region referred to as the triple-phase boundary (TPB), in contact with the vapor, particle and nanowire.

The excess energy formed when dividing a bulk material in two parts is known as surface energy γ. To a first approximation it is proportional to the density of dangling bonds, but the bond strength and influence from neighboring atoms should also be taken into consideration [59].

Similarly to a surface energy, when two different surfaces form an interface, an excess energy known as interfacial energy forms. During nucleation, a small nucleus of the solid phase forms, and consequently also interfacial energies between the nucleus and the connected phases. If the interfacial energy between nucleus and particle is lower than that of the nucleus and vapor this would result in a lowering of the total surface energy of the formed nucleus.

Chapter 5

Thermal compaction of metal nanoparticles

The spark discharge generator (SDG) is used to develop new alternative seed particles to grow nanowires from. For this purpose it is important that the purity, size and shape of the particles are well controlled. In table 5.1, materials developed by the SDG and used for preliminary nanowire growth studies are presented. The table includes electrode material, electrode purity, bulk melting temperature T_m and compaction temperature T_c for 80 nm agglomerates. At T_c, further increasing the sintering temperature will not result in a more compact nanoparticle.

This chapter covers how the compaction of nanoparticles is performed to develop spherical nanoparticles, and the development of palladium nanoparticles used for Paper II is presented in detail. Depending on material (see * in table 5.1), the compaction can be improved by introducing hydrogen when generating the particles. This is demonstrated in Paper I, where hydrogen has a significant effect on the compaction behaviour for Co and Bi, but none for Au.

Table 5.1: List of developed nanoparticle materials used for nanowire growth. The electrode purity, bulk melting temperature T_m, and observed compaction temperature T_c for particles generated in high purity nitrogen $T_c(N_2)$ and for particles generated in a nitrogen-hydrogen mixture $T_c(H_2)$. * Only generated in high purity nitrogen.

Material	Purity [%]	T_m [°C]	$T_c(H_2)$ [°C]	$T_c(N_2)$ [°C]
Gold	99.95	1064	375	375
Palladium*	99.95	1555	400	—
Cobalt	99.99	1495	600	> 800
Bismuth	99.999	272	400	600

1 Sintering scans and TEM verification

In figure 5.1 the compaction behaviour of Pd, Co and Au is presented. The noble metals, Au and Pd exhibit similar compaction behaviour, compacting rapidly already at low temperatures, and reaching the compaction temperature already at ($\sim 400 - 500$ °C). However, Co does not compact fully within the observable temperature range, ($20 - 900$ °C). In section 2 it is shown that the compaction of Co nanoparticles can be improved by introducing hydrogen during the particle generation. However, first I will focus upon the compaction of Pd nanoparticles, used to seed GaAs nanowires in Paper II.
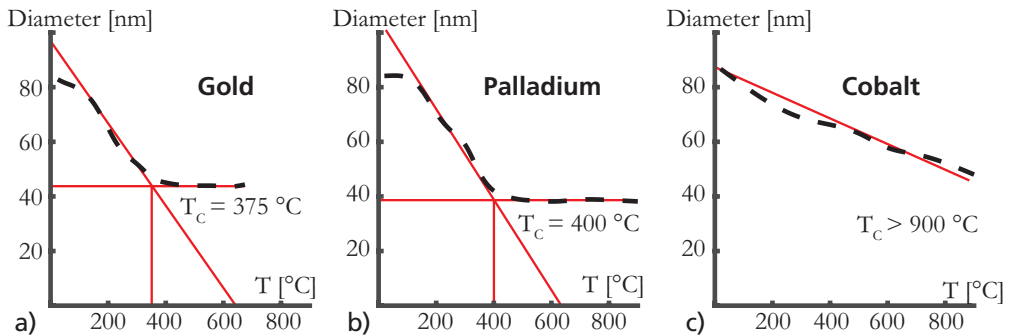

Figure 5.1: Mobility size diameter for 80 nm agglomerate nanoparticles after sintering at different temperatures for a) Au, b) Pd, c) Co.

TEM investigations presented in figure 5.2 verifies that Pd nanoparticles are: a) highly agglomerated when sintered at room temperature (20 °C), b) relatively compact but polycrystalline slightly above the compaction temperature (500 °C), and c) monocrystalline and faceted if sintered at very high temperatures (1150 °C).

Too high sintering temperatures might result in evaporation of material and problems with multiply charged particles. Singly charged particles are essential to control particle size and particle concentration. However, at high sintering temperatures, thermal charging will result in an altered particle charge distribution [60, 61]. Multiply charged particles have a mobility diameter that is smaller than their geometric diameter and the number of particles is overestimated by the electrometer. This is because both the DMA and electrometer assumes singly charged particles in our system. Furthermore, due to the lower mobility diameter the electrostatic precipitator will deposit multiply charged particles in a smaller area than singly charged particles. For these reasons, it is important not to compact particles at too high sintering temperatures [61].
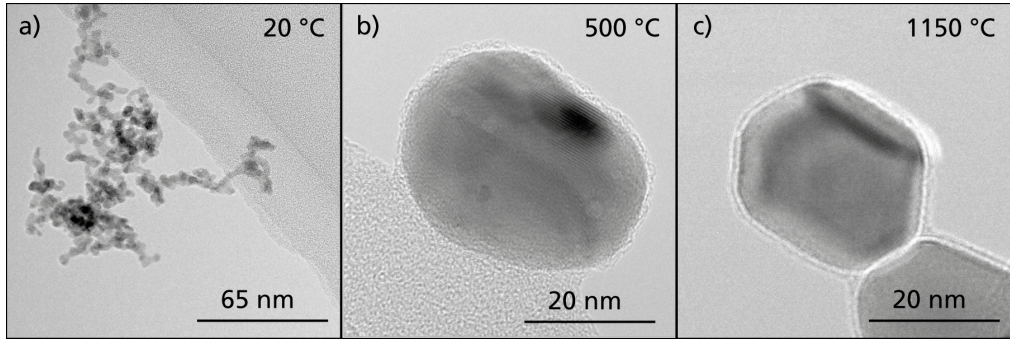
Figure 5.2: TEM images of a) the 80 nm Pd agglomerate, that compacts completely at 500 °C (above T_c), and at c) 1150 °C internal restructuring and facet reshaping is observed.

2 Hydrogen to improve compaction

Palladium and gold are noble metals and do not readily oxidise. To prevent oxidation of base metals, a reducing carrier gas consisting of 95 % N_2 and 5 % H_2 is used. In paper I we show that hydrogen has a significant effect on the compaction behaviour for Co and Bi, but as expected, no effect is observed for Au.

In figure 5.3 a) Co nanoparticles generated and sintered using the two different carrier gases are compared. It is clear that T_c is much lower for the hydrogen mixture ($T_c \approx 600$ °C), compared to the pure nitrogen ($T_c \geq 800$ °C). In figure 5.3 b) and c) particles deposited at 700 °C are compared for the two gas compositions. The particle generated in nitrogen is agglomerated, whereas the particle generated in the hydrogen mixture is fairly compact.

Similar effects occur with Bi nanoparticles (see Paper I) and Sn nanoparticles (not presented). However, the compaction of Au is not affected when adding hydrogen, as is presented in figure 5.4. The two mobility diameter curves are almost identical and the TEM images of particles compacted at 500 °C are very similar, regardless of gas type.

2.1 Oxidation

It is plausible that hydrogen prevents the formation of oxides or reduces formed oxides in the early stages of particle generation. This is supported by previous work on Ni and Pt nanoparticles [62], where hydrogen was shown to lower the kinetic barrier for restructuring (compaction) for Ni particles but not for Pt nanoparticles. However, further work is required to investigate how it extends to additional base metals.

Most metals oxidise readily in air, and very low oxygen levels are enough for the oxide to be
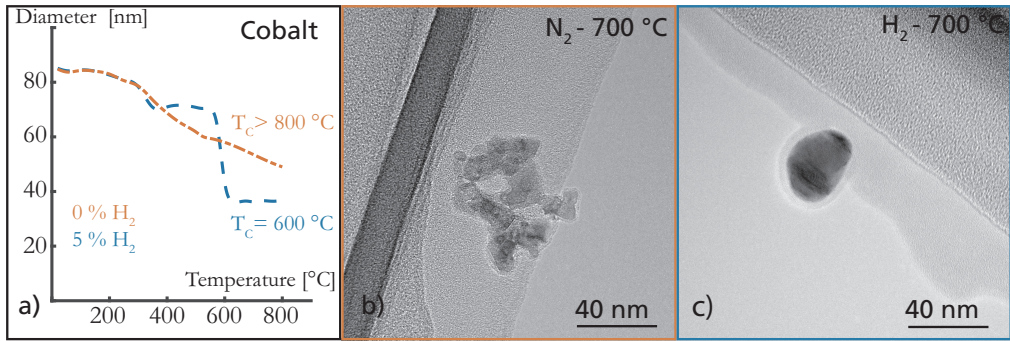
Figure 5.3: Cobalt compaction is compared for the two gases 99.999 % N_2, and 95 % N_2 and 5 % H_2. a) With hydrogen, the compaction temperature is low $\approx$ 600 °C, compared to without hydrogen > 900 °C. Particle deposited at 700 °C are less compact when generated b) without H_2 compared to when generated c) with H_2.

thermodynamically stable. We know that the SDG has small residues of oxygen and water adsorbed on the inner walls, that are difficult to remove without resorting to high-vacuum techniques and prolonged baking. However, even if possible it interferes with the purpose of the system, to be a highly customizable and portable system opened to the ambient atmosphere at a daily to weekly basis.

Post production the particles are expected to oxidise as they are transferred in air to the electron microscope or MOCVD machine. However, oxidation is often reversible, and if < 5 % H_2 in the SDG is sufficent to reduce oxides or prevent oxidation it is likely that 100 % H_2 in the MOCVD machine can reduce it again. Furthermore, even if most metals oxidise, some metals (e.g. Ti and Al) form thin surface oxides that prevents further oxidation [38, p. 876-878]. This, and the contribution of kinetic effects are highly interesting aspects that will surely require additional research.
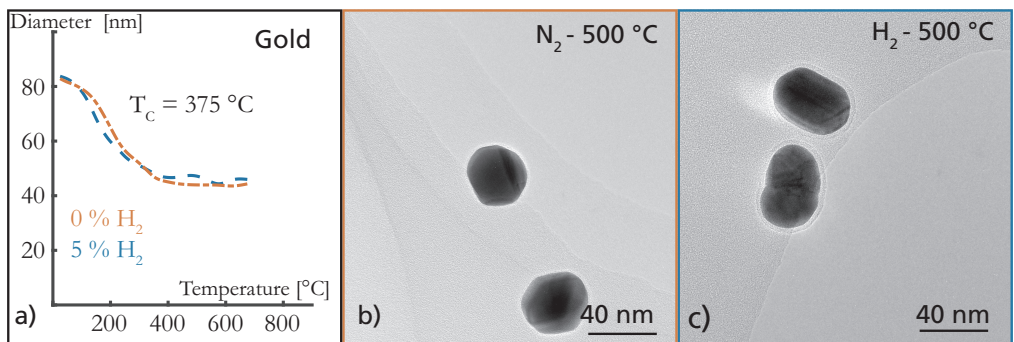
Figure 5.4: Gold nanoparticles compacted at 500 $^\circ$C are compared for the two gases 99.999 % N_2, and 95 % N_2 and 5 % H_2. a) The mobility diameter for the two gases are compared, b) only N_2 yields similar particles to when generated c) with H_2.

Chapter 6

The role of the seed particle - Pd seeded GaAs

To investigate the effect of the seed particle material, the nanowire properties (e.g. morphology and growth rate) are compared within growth series. A growth series consists of a set of growth runs, where growth parameters (e.g. growth temperature and precursor flows) are changed systematically.

This chapter begins with explaining how V/III ratio and growth temperature are important growth parameters. Thereafter, results from paper II are summarised, where Pd seeded GaAs nanowires from a wide growth parameter space are presented, covering V/III ratios between $0.4-63$, and growth temperatures between $350-600\,°C$. The nanowire morphology is controllable with growth parameters, where unstable growth of "curly" nanowires is predominant for all growth settings except high growth temperatures and low V/III ratios. For such growth settings, stable growth of "vertical" and "inclined" nanowires are promoted and growth of curly nanowires is suppressed. In Paper II we proposed that the shift in morphology is due to a difference in particle phase. Therefore, this chapter will appropriately close with a discussion around the particle phase.

1   Effect of V/III ratio and growth temperature

The growth rate of binary III-V semiconductors can be controlled by adjusting the effective V/III ratio. The effective V/III ratio determines which precursor at the growth interface that limits the growth rate, and to a first approximation it follows the same trends as the relative precursor flows (referred to as nominal V/III ratio). However, the two are not equivalent,

due to differences in precursor decomposition and diffusion.

A V/III series can be constructed in order to tune the effective V/III ratio in three ways: fixing the group III precursor flow and varying the group V precursor flow, varying the group III precursor flow and fixing the group V precursor flow, or varying group III and V simultaneously while maintaining a constant total flow. In paper II we show that the nominal V/III ratio controls the growth rate of Pd seeded GaAs nanowires at low growth temperature (Paper II FIG. 8), and at a higher growth temperature the V/III ratio also controls the nanowire morphology (Paper II FIG. 7 and 8).

Temperature affects kinetic processes (e.g. decomposition and nucleation) and thermodynamic equilibrium (e.g. solubility, vapor pressure and chemical potential). Therefore, growth at different temperatures, (but same nominal V/III ratio) can yield entirely different nanowires. In paper II, temperature series at a low nominal V/III ratio (V/III = 0.8), and high nominal V/III ratio (V/III = 24) are presented. Both series exhibit fewer nanowires at higher growth temperatures, see figure 6.1. As the initial particle density is the same within a growth series, this suggests that nucleation of nanowires is hindered at higher growth temperatures. Furthermore, the temperature series at the lower V/III ratio shows a change in nanowire morphology, from curly nanowires at low growth temperatures to vertical nanowires at high growth temperatures. This is unfortunate as stable growth of vertical and inclined nanowires is only observed at growth temperatures where nucleation is poor.
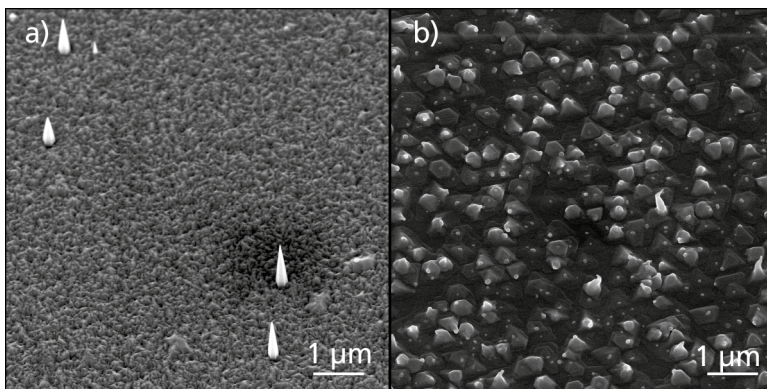
Figure 6.1: Pd seeded GaAs nanowires have difficulties with nucleation at high growth temperatures (600 °C) and the morphology is mostly vertical at low V/III ratios a) V/III = 0.8, and curly at higher V/III ratios b) V/III = 22. (Note, the growth time in a) is longer, due to throttled growth rate at low V/III).

Additional V/III series performed at low and high growth temperatures suggested that the low V/III ratio promotes vertical growth and a higher Ga incorporation into the nanoparticle. Compositional analyses on seed particles post growth revealed a high Ga incorporation (60 − 80 at %) for growth temperatures above 580 °C and V/III below 1. For

other growth conditions, the Ga incorporation was consistently $40 - 50$ at %, (paper II table II). The Ga incorporation controls the melting temperature of the formed alloy, where a high incorporation drastically decreases the melting point. Although the post-growth composition is not equivalent to the composition during growth, it is a good first approximation and can give information about compositional trends. A particle with a composition similar to the high Ga incorporation could be liquid during growth temperatures ($\sim 550 - 900$ °C), while a particle with a composition similar to the lower Ga incorporation could not (~ 1000 °C) [63].

2   Curly nanowires - Unstable growth

Curly nanowires are categorised by their unstable growth direction, forming a twisting nanowires that when grown long enough often "curls" around itself. In figure 6.2 a) a SEM image of typical curly nanowires is shown. The crystal structure of such nanowires consists of a complicated arrangement of zincblende twinning structures, and an occasional anisotropic nanoparticle/nanowire interface, see figure 6.2 b). The unstable growth direction of a curly nanowire makes even basic properties such as length and radial growth non-trivial to quantify. However, by comparing SEM images side-by-side it is possible to make qualitative comparisons in order to establish trends.

Previous work on in-situ TEM of nanowire growth from solid particles has shown that growth occurs via a step flow at the seed particle/nanowire interface [64, 65]. Growth in a $\langle 1\,1\,1\rangle$ direction is therefore proposed to occur by the completion of a bi-layer. With an anisotropic particle/wire interface a bi-layer cannot be completed with a single step flow. Instead multiple step flows on different facets is required, potentially destabilising the growth direction by competition between several growth directions.

3   Vertical and inclined nanowires - Stable growth

In figure 6.3, SEM images of a) vertical and b) inclined nanowires are shown. Assuming epi-taxial growth, the vertical nanowires are growing in a $\langle 1\,1\,1\rangle$B growth direction, although in order to prove epitaxial growth cross-sectional TEM analysis of the substrate/nanowire interface is required. However, TEM analyses of samples mainly consisting of vertical nanowires confirms growth in a $\langle 1\,1\,1\rangle$ direction, which strongly supports the conclusion that vertical nanowires are epitaxial to the GaAs $(1\,1\,1)$B substrate. In figure 6.3 c) a TEM image of a vertical Pd seeded GaAs nanowire with a mixed crystal structure, characteristic for unoptimized $\langle 1\,1\,1\rangle$ growth, is shown. The mixed crystal structure is apparent from the streaking lines in the diffraction pattern, presented in the inset.
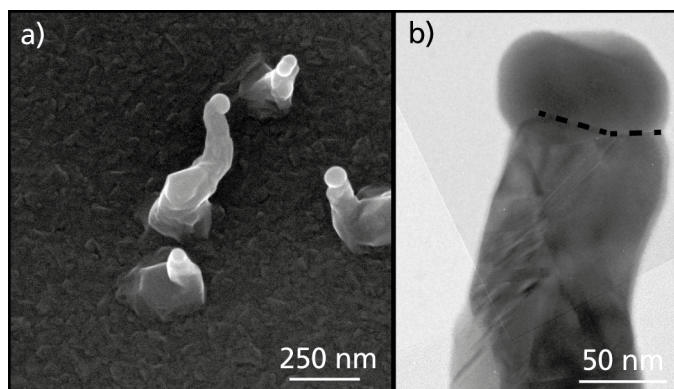
Figure 6.2: a) Typical curly Pd seeded GaAs nanowires imaged by SEM at 30° b) TEM of a curly nanowire with a twinned zincblende structure and an anisotropic particle/nanowire interface.

The seed particle/nanowire interface controls how the subsequent layer is built. Therefore, the interface has a large effect on both growth direction and the introduction of stacking-faults. For growth in a $\langle 1\,1\,1 \rangle$ direction, the growth interface is often perpendicular to the growth direction and stacking-faults are easily introduced as new layers are added. However, if growth occurs in a different growth direction (or rather the particle/nanowire interface is a non-(111)), stacking-faults or defects cannot form in a single flow.

In figure 6.3 d) an inclined nanowire with a defect-free zinc blende structure is observed. By comparing the diffraction pattern to the nanowire morphology a $\langle 1\,0\,0 \rangle$ growth direction is deduced. The crystal structure is defect free zinc-blende, even with a $(1\,1\,1)$ particle/wire interface. However, the interface could have changed during the last moments of growth. When turning off the precursor flows and cooling down, the particle may shrink in size as the Ga reservoir in the particle is used up for growth, forming a "neck-region" with a smaller wire diameter beneath the particle [56]. For this to occur, a continued AsH_3 supply during cooldown is usually necessary. In Paper II, the growth of Pd seeded GaAs nanowires was terminated with cooling down without AsH_3 (and TMG), which means that growth during cooldown was limited, but cannot be excluded.Furthermore, not all inclined nanowires in Paper II were defect free zinc-blende, but some were riddled with inclined stacking-faults (not presented). A plausible explanation would be a $(1\,1\,1)$ particle/wire interface.

Finally, as discussed in paper II the particle size post-growth is not always consistent with an initial 40 nm Pd nanoparticle. This is also easily observed in figure 6.3, where a ~ 70 nm particle is seen in b) and 25 nm particle in d).
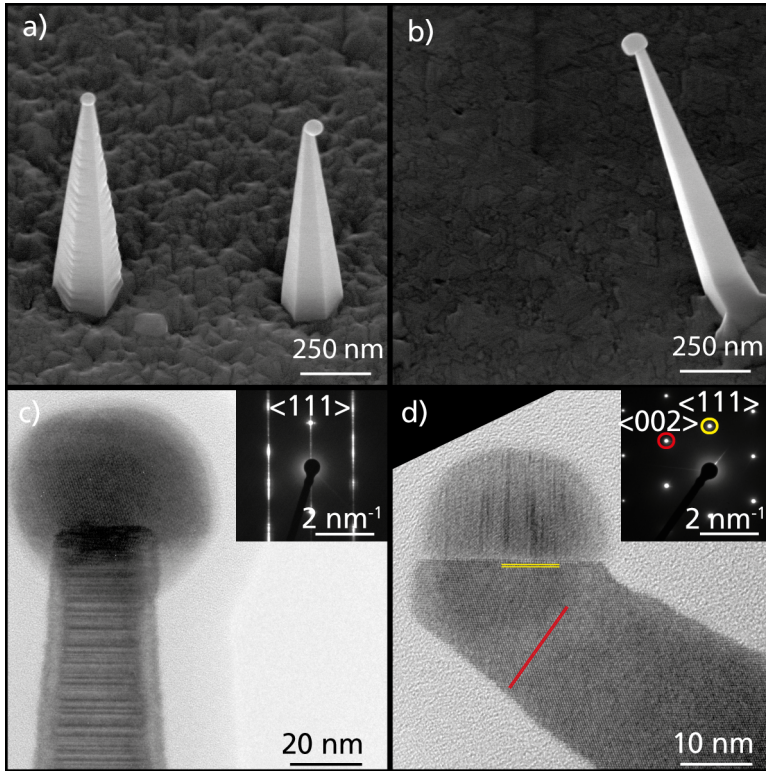
Figure 6.3: Pd seeded GaAs nanowires in stable growth directions, 30 ° tilted SEM images of a) vertical, b) inclined. The crystal structure and growth direction is determined by TEM: c) vertical nanowire grown in ⟨1 1 1⟩ with a mixed crystal structure, d) inclined nanowire grown in ⟨1 0 0⟩ with defect-free zinc-blende.

4   The particle phase

In Paper II we proposed that the curly Pd seeded GaAs nanowires are grown from a solid nanoparticle, according to the vapor-solid-solid (VSS) mechanism [56]. The vertical and inclined nanowires are instead grown from a liquid nanoparticle, mediated by the vapor-liquid-solid (VLS) mechanism [52]. This claim was supported mainly by two observations, the relative nanowire growth rate and the post-growth particle composition.

The growth rate of curly nanowires was lower than for straight nanowires. Across the entire explored growth parameter space, whenever curly nanowires co-existed with vertical or inclined nanowires, the curly nanowires were shorter and smaller than the straight nanowires. Not only was the apparent length of the nanowires different, but also the volume of the nanowire. This is clear evidence that the two morphologies have different growth rates, suggesting different growth mechanisms. Previous work has observed co-existing growth from solid and liquid nanoparticles [6, 66, 67]. Furthermore, the same work reports of

a slower growth rate for growth from solid nanoparticles. This can be explained by, for example, lower bulk diffusion in solids and lower vapor deposition rate to a solid surface compared to a liquid surface.

The post-growth composition ($40 - 50$ at % Ga) of particles from curly nanowires corresponds to an alloy expected to be solid (M_p(PdGa) $\approx 1000\ ^{\circ}$C) for typical growth temperatures. Palladium has a high melting point, (M_p(Pd) $\approx 1550\ ^{\circ}$C), and a very high Ga incorporation ($> 80\%$) is required for forming an alloy that is liquid during growth. Compositional analysis revealed a high Ga incorporation ($60 - 80$ at %) for growth temperatures above 580 $^{\circ}$C and V/III below 1, growth settings where vertical nanowires were predominant. The particle composition is not necessarily the same during growth, but by cooling down the sample in H_2 the Ga reservoir is not as easily depleted [56]. Furthermore, it is well known that effects such as undercooling [55], formation of metastable phases [68], and size dependent melting point depression [69] may contribute to liquid phases not predicted by the phase diagram of the bulk. However, it is unlikely that these effects are pronounced enough to form a liquid alloy for the low Ga content particles.

Chapter 7

Concluding remarks and outlook

Various metals are now developed for seeding nanowires, and some of these materials (Bi, Co) rely on the "hydrogen assisted compaction" method treated in Paper I, whereas other materials (Au, Pd) are simpler and do not require hydrogen during generation. Pd seeded GaAs nanowires grow with two distinct morphologies, straight nanowires or curly nanowires. I propose that straight nanowires are promoted by a liquid nanoparticle, facilitated by a higher Ga incorporation, whereas curly nanowires are promoted by a anisotropic solid nanoparticle, which is unable to form a stable growth interface. This might be applicable to other seed particle materials, that form similar particle/wire interfaces when solid and liquid.

The goal of my PhD is to determine how specific seed particle properties affect nanowire properties. I choose to do this by comparing the growth from similar and dissimilar seed particle materials. Due to the large effect of particle phase the elements of interest are divided into low melting point materials and high melting point materials. Low melting point materials are common in groups III-V (e.g. Ga, In, Sn, Pb, Sb and Bi). These elements are interesting as they will almost certainly be liquid during growth, and if incorporated into a III/V or IV nanowire they may act as a dopant or alter the band structure. Higher melting point materials can for example be found among the transition metals in close proximity to Pd and Au (Co, Rh, Ni, Pt, Cu and Ag). When alloying with group III elements they lower their melting temperature, and the phase may change from solid to liquid (at growth temperatures) depending on group III incorporation. However, most of these materials require high group III incorporation (similar to Pd) to become liquid. By systematically studying the growth from both low and high melting point materials it will be possible to study the effect of particle phase. The aims are to learn how to control the particle phase, how it affects the nanowire properties and ultimately to make the choice of seed material as clear and straight forward as the choice of semiconductor material.

References

References

[1] K. A. Dick. A review of nanowire growth promoted by alloys and non-alloying elements with emphasis on Au-assisted III–V nanowires. *Progress in Crystal Growth and Characterization of Materials*, 54(3-4):138–173, sep 2008.

[2] P. Nguyen, H. T. Ng, and M. Meyyappan. Catalyst metal selection for synthesis of inorganic nanowires. *Advanced Materials*, 17(14):1773–1777, 2005.

[3] M. Tornberg, E. K. Mårtensson, R. R. Zamani, S. Lehmann, K. A. Dick, and S. G. Ghalamestani. Demonstration of Sn-seeded GaSb homo- and GaAs – GaSb heterostructural nanowires. *Nanotechnology*, 27(17):0, 2016.

[4] H. Xu, Y. Wang, Y. Guo, Z. Liao, and Q. Gao. Defect-free< 110> zinc-blende structured InAs nanowires catalyzed by palladium. *Nano letters*, 12:5744–5749, 2012.

[5] I. Regolin, V. Khorenko, W. Prost, F. J. Tegude, D. Sudfeld, J. Kästner, G. Dumpich, K. Hitzbleck, and H. Wiggers. GaAs whiskers grown by metal-organic vapor-phase epitaxy using Fe nanoparticles. *Journal of Applied Physics*, 101(5):1–5, 2007.

[6] S. Heun, B. Radha, D. Ercolani, G. U. Kulkarni, F. Rossi, V. Grillo, G. Salviati, F. Beltram, and L. Sorba. Coexistence of vapor-liquid-solid and vapor-solid-solid growth modes in Pd-assisted InAs nanowires. *Small (Weinheim an der Bergstrasse, Germany)*, 6(17):1935–41, sep 2010.

[7] S. Heun, B. Radha, D. Ercolani, G. U Kulkarni, F. Rossi, Vincenzo Grillo, Giancarlo S., F. Beltram, and L. Sorba. Pd-assisted growth of InAs nanowires. *Crystal Growth and Design*, 10(9):4197–4202, sep 2010.

[8] K. Hillerich, D. S. Ghidini, K. A. Dick, K. Deppert, and J. Johansson. Cu particle seeded InP-InAs axial nanowire heterostructures. *Physica Status Solidi - Rapid Research Letters*, 7(10):850–854, 2013.

[9] R. Sun, D. Jacobsson, I-J. Chen, M. Nilsson, C. Thelander, S. Lehmann, and K. A. Dick. Sn-Seeded GaAs Nanowires as Self-Assembled Radial p-n Junctions. *Nano letters*, 15(6):3757–3762, jun 2015.

[10] D. E. Perea, E. R. Hemesath, E. J. Schwalbach, J. L. Lensch-Falk, P. W. Voorhees, and L. J. Lauhon. Direct measurement of dopant distribution in an individual vapour – liquid – solid nanowire. *Nature nanotechnology*, 4(March):315–319, 2009.

[11] E. R. Hemesath, D. K. Schreiber, E. B. Gulsoy, C. F. Kisielowski, A. K. Petford-Long, P. W. Voorhees, and L. J. Lauhon. Catalyst incorporation at defects during nanowire growth. *Nano letters*, 12(1):167–71, jan 2012.

[12] J. E. Allen, E. R. Hemesath, D. E. Perea, J. L. Lensch-Falk, Z. Y. Li, F. Yin, M. H. Gass, P. Wang, A. L. Bleloch, R. E. Palmer, and L. J. Lauhon. High-resolution detection of Au catalyst atoms in Si nanowires. *Nature nanotechnology*, 3(3):168–73, mar 2008.

[13] M. Bar-Sadan, J. Barthel, H. Shtrikman, and L. Houben. Direct imaging of single Au atoms within GaAs nanowires. *Nano letters*, 12(5):2352–6, may 2012.

[14] H. Shtrikman, R. Popovitz-Biro, A. V. Kretinin, and P. Kacman. GaAs and InAs Nanowires for Ballistic Transport. *IEEE Journal of Selected Topics in Quantum Electronics*, 17(4):922–934, 2011.

[15] E. Koren, G. Elias, A. Boag, E. R. Hemesath, L. J. Lauhon, and Y. Rosenwaks. Direct Measurement of Individual Deep Traps in Single Silicon Nanowires. *Nano Letters*, 11:2499–2502, 2011.

[16] H. Schift. Nanoimprint lithography: An old story in modern times? A review. *Journal of Vacuum Science & Technology B: Microelectronics and Nanometer Structures*, 26(2):458, 2008.

[17] B. O. Meuller, M. E. Messing, D. L. J. Engberg, A. M. Jansson, L. I. M. Johansson, S. M. Norlén, N. Tureson, and K. Deppert. Review of Spark Discharge Generators for Production of Nanoparticle Aerosols. *Aerosol Science and Technology*, 46(11):1256–1270, nov 2012.

[18] D. L. Smith. *Thin-film deposition : principles and practice.* New York : McGraw-Hill, cop. 1995, 1995.

[19] S. Schwyn, E. Garwin, and A. Schmidt-Ott. Aerosol generation by spark discharge. *Journal of Aerosol Science*, 19(5):639–642, 1988.

[20] T. V. Pfeiffer, J. Feng, and A. Schmidt-Ott. New developments in spark production of nanoparticles. *Advanced Powder Technology*, 25(1):56–70, jan 2014.

[21] R. L. Watters, J. R. DeVoe, F. H. Shen, J. A. Small, and R. B. Marinenko. Characteristics of Aerosols Produced by the Spark Discharge. *Analytical Chemistry*, 61(17):1826–1833, 1989.

[22] C. Roth, G. A. Ferron, E. Karg, B. Lentner, G. Schumann, S. Takenaka, and J. Heyder. Generation of Ultrafine Particles by Spark Discharging. *Aerosol Science and Technology*, 38(3):228–235, 2004.

[23] N. S. Tabrizi, Q. Xu, N. M. Van Der Pers, U. Lafont, and A. Schmidt-Ott. Synthesis of mixed metallic nanoparticles by spark discharge. *Journal of Nanoparticle Research*, 11:1209–1218, 2009.

[24] V. A. Vons, L. C. P. M. Smet, D. Munao, A. Evirgen, E. M. Kelder, and A. Schmidt-Ott. Silicon nanoparticles produced by spark discharge. *Journal of Nanoparticle Research*, 13(10):4867–4879, jun 2011.

[25] J. Kim and J. Chang. Generation of metal oxide aerosol particles by a pulsed spark discharge technique. *Journal of Electrostatics*, 63(6-10):911–916, jun 2005.

[26] N. S. Tabrizi. *Generation of nanoparticles by spark discharge.* PhD thesis, Technische Universiteit Delft, 2009.

[27] E. Kuffel, W.S. Zaengl, and J. Kuffel. *High Voltage Engineering - Fundamentals.* Newnes, Oxford, 2000.

[28] E. Hontañón, J. M. Palomares, X. Guo, R. Engeln, H. Nirschl, and F. E. Kruis. Influence of the inter-electrode distance on the production of nanoparticles by means of atmospheric pressure inert gas dc glow discharge. *Journal of Physics D: Applied Physics*, 47(41):415201, 2014.

[29] A. Schmidt-ott and T. V. Pfeiffer. WO2013115644A11.pdf, 2013.

[30] R. Reinmann and M. Akram. Temporal investigation of a fast spark discharge in chemically inert gases. *Journal of Physics D: Applied Physics*, 30(7):1125–1134, 1999.

[31] T. E. Itina and A. Voloshko. Nanoparticle formation by laser ablation in air and by spark discharges at atmospheric pressure. *Applied Physics B*, 113:473–478, 2013.

[32] J. Feng, G. Biskos, and A. Schmidt-Ott. Toward industrial scale synthesis of ultrapure singlet nanoparticles with controllable sizes in a continuous gas-phase process. *Scientific Reports*, 5(February):15788, 2015.

[33] J. Borra. Nucleation and aerosol processing in atmospheric pressure electrical discharges: powders production, coatings and filtration. *Journal of Physics D: Applied Physics*, 39(2):R19–R54, 2006.

[34] A. P. Weber and S. K. Friedlander. In situ determination of the activation energy for restructuring of nanometer aerosol agglomerates. *Journal of Aerosol Science*, 28(2):179–192, 1997.

[35] B. Y. H. Liu and D. Y. H. Pui. Electrical neutralization of aerosols. *Journal of Aerosol Science*, 5(5):465–472, 1974.

[36] A. Wiedensohler. An approximation of the bipolar charge distribution for particles in the submicron size range. *Journal of Aerosol Science*, 19(3):387–389, 1988.

[37] E. O. Knutson and K. T. Whitby. Aerosol classification by electric mobility: apparatus, theory, and applications. *Journal of Aerosol Science*, 6(6):443–451, 1975.

[38] W. Wright D. Askeland, P. Fulay. *The Science and Engineering of Materials*. Chapman and Hall, London, 6 edition, 2011.

[39] A. Schmidt-Ott. New approaches to in situ characterization of ultrafine agglomerates. *Journal of Aerosol Science*, 19(5):553–563, 1988.

[40] M. N. A. Karlsson, K. Deppert, L. S. Karlsson, M. H. Magnusson, J. O. Malm, and N. S. Srinivasan. Compaction of agglomerates of aerosol nanoparticles: A compilation of experimental data. *Journal of Nanoparticle Research*, 7(1):43–49, 2005.

[41] M. E. Messing, R. Westerström, B. O. Meuller, S. Blomberg, J. Gustafson, J. N. Andersen, E. Lundgren, R. van Rijn, O. Balmes, H. Bluhm, and K. Deppert. Generation of Pd Model Catalyst Nanoparticles by Spark Discharge. *The Journal of Physical Chemistry C*, 114(20):9257–9263, may 2010.

[42] D. B. Williams and C. B. Carter. *The Transmission Electron Microscope*. Springer, 2009.

[43] U. W. Pohl. *Epitaxy of Semiconductors: Introduction to Physical Principles*. Berlin ; Heidelberg : Springer, cop. 2013, 2013.

[44] P. Krogstrup, N. L. B. Ziino, W. Chang, S. M. Albrecht, M. H. Madsen, E. Johnson, J. Nygård, C. M. Marcus, and T. S. Jespersen. Epitaxy of semiconductor–superconductor nanowires. *Nature Materials*, 14(4):400–406, 2015.

[45] P. W. Atkins and L. Jones. *Chemical principles : the quest for insight*. New York : W.H. Freeman, cop. 2008, 2008.

[46] C.A. Larsen, N.I. Buchan, S. H. Li, and G. B. Stringfellow. Decomposition mechanisms of trimethylarsine. *Journal of Crystal Growth*, 102(1-2):117–125, 1990.

[47] K. Ikejiri, J. Noborisaka, S. Hara, J. Motohisa, and Takashi Fukui. Mechanism of catalyst-free growth of GaAs nanowires by selective area MOVPE. *Journal of Crystal Growth*, 298:616–619, 2007.

[48] K. W. Kolasinski. Catalytic growth of nanowires: Vapor-liquid-solid, vapor-solid-solid, solution-liquid-solid and solid-liquid-solid growth. *Current Opinion in Solid State and Materials Science*, 10(3-4):182–191, 2006.

[49] Wei Lu and Charles M Lieber. Semiconductor nanowires. *Journal of Physics D: Applied Physics*, 39(21):R387–R406, nov 2006.

[50] S. J. May, J.-G. Zheng, B. W. Wessels, and L. J. Lauhon. Dendritic Nanowire Growth Mediated by a Self-Assembled Catalyst. *Advanced Materials*, 17(5):598–602, mar 2005.

[51] K. P. DE JONG and K. W. GEUS. Carbon Nanofibers: Catalytic Synthesis and Applications. *Catalysis Reviews*, 42(4):481–510, feb 2007.

[52] R. S. Wagner and W. C. Ellis. Vapor-liquid-solid mechanism of single crystal growth. *Applied Physics Letters*, 4(5):89–90, 1964.

[53] E. I. Givargizov. Fundamental aspects of VLS growth. *Journal of Crystal Growth*, 31(C):20–30, 1975.

[54] K. A. Dick, K. Deppert, T. Mårtensson, B. Mandl, L. Samuelson, and W. Seifert. Failure of the vapor-liquid-solid mechanism in Au-assisted MOVPE growth of InAs nanowires. *Nano letters*, 5(4):761–4, apr 2005.

[55] S Kodambaka, J Tersoff, M C Reuter, and F M Ross. Germanium nanowire growth below the eutectic temperature. *Science (New York, N.Y.)*, 316(5825):729–732, 2007.

[56] A. I. Persson, M. W. Larsson, S. Stenström, B. J. Ohlsson, L. Samuelson, and L. R. Wallenberg. Solid-phase diffusion mechanism for GaAs nanowire growth. *Nature materials*, 3(10):677–681, oct 2004.

[57] B. A. Wacaser, M. C. Reuter, M. M. Khayyat, C. Y. Wen, R. Haight, S. Guha, and F. M. Ross. Growth system, structure, and doping of aluminum-seeded epitaxial silicon nanowires. *Nano Letters*, 9(9):3296–3301, 2009.

[58] E. Clouet. Modeling of Nucleation Processes. *ASM Handbook*, 22A:203–219, 2009.

[59] N. V. Sibirev, M. A.. Timofeeva, A.. D. Bol'shakov, M. V. Nazarenko, and V. G. Dubrovskii. Surface energy and crystal structure of nanowhiskers of III–V semiconductor compounds. *Physics of the Solid State*, 52(7):1531–1538, 2010.

[60] M. H. Magnusson, K. Deppert, J. Malm, J. Jan-Olov Bovin, and L. Samuelson. Gold nanoparticles: Production, reshaping, and thermal charging. *Journal of Nanoparticle Research*, 1:243–251, 1999.

[61] M. N. A. Karlsson, K. Deppert, B. A. Wacaser, L. S. Karlsson, and J. O. Malm. Size-controlled nanoparticles by thermal cracking of iron pentacarbonyl. *Applied Physics A: Materials Science and Processing*, 80(7):1579–1583, 2005.

[62] M. Seipenbusch, A. P. Weber, A. Schiel, and G. Kasper. Influence of the gas atmosphere on restructuring and sintering kinetics of nickel and platinum aerosol nanoparticle agglomerates. *Journal of Aerosol Science*, 34(12):1699–1709, 2003.

[63] B Predel. Ga - Pd (Gallium - Palladium). In *Landolt-Brönstein*, chapter IV- Physic, pages 57–59. Springer Materials, new series edition, 1996.

[64] S. Hofmann, R. Sharma, C. T. Wirth, F. Cervantes-Sodi, C. Ducati, T. Kasama, R. E. Dunin-Borkowski, J. Drucker, P. Bennett, and J. Robertson. Ledge-flow-controlled catalyst interface dynamics during Si nanowire growth. *Nature materials*, 7(5):372–5, may 2008.

[65] C.-Y. Wen, J. Tersoff, M. C. Reuter, E. A. Stach, and F. M. Ross. Step-flow kinetics in nanowire growth. *Physical Review Letters*, 105(19):1–4, 2010.

[66] K. Hillerich, K. A. Dick, M. E. Messing, K. Deppert, and J. Johansson. Simultaneous growth mechanisms for Cu-seeded InP nanowires. *Nano Research*, 5(5):297–306, 2012.

[67] HY Xu, YN Guo, ZM Liao, and Wen Sun. Catalyst size dependent growth of Pd-catalyzed one-dimensional InAs nanostructures. *Applied Physics Letters*, 102(203108):1–5, 2013.

[68] A. D. Gamalski, J. Tersoff, R. Sharma, C. Ducati, and S. Hofmann. Formation of metastable liquid catalyst during subeutectic growth of germanium nanowires. *Nano Letters*, 10(8):2972–2976, 2010.

[69] Q. Jiang, S. Zhang, and M. Zhao. Size-dependent melting point of noble metals. *Materials Chemistry and Physics*, 82(1):225–227, sep 2003.

Scientific publications

Paper 1

Hydrogen assisted compaction of spark discharge generated nanoparticles

R. T. Hallberg[1], L. Ludvigsson[1], Bengt. O. Meuller[1], K. A. Dick[1,2], and M. E. Messing[1]

[1]Solid State Physics, Lund University, Box 118, S-221 00 Lund, Sweden
[2]Centre for Analysis and Synthesis, Lund University, Box 124, S-221 00 Lund, Sweden

Abstract

Agglomeration results in unstructured nanoparticles unsuitable for many applications. Thermal compaction in the gas-phase can be performed in order to reshape agglomerates into spherical nanoparticles. However, easily oxidised metals are more resistant to thermal compaction due to the formation of surface contaminations and the high melting point of oxides. By introducing hydrogen at the particle formation we show that the compaction of Co and Bi nanoparticles is improved significantly, whereas the compaction of Au nanoparticles is unaffected. Co nanoparticles generated in a hydrogen mixture underwent rapid compaction at 600 °C forming spherical nanoparticles, wheras particles generated in pure nitrogen compacted slowly, forming faceted and fractal particles. Bi nanoparticles required compaction temperatures above the melting point for both gas compositions, but the compaction occurs earlier and the particle shape is more uniform when generated in the hydrogen mixture. We propose that hydrogen hinders the formation of oxides at particle formation, resulting in improved compaction compared to particles generated in only nitrogen. This method can be applied to other aerosol generation systems, in order to improve the generation of size controlled nanoparticles of base metals.

1 Introduction

Production of nanoparticles with controlled shape and composition is required for many applications, including semiconductor nanostructures,[1] catalysis,[2] medi-cine[3,4] and hydrogen storage.[5] A promising production method is via a spark discharge generator (SDG),[6] a technique enabling production of nanoparticles of basically any non-insulating material that can be shaped into an electrode.[7] In SDG the particle purity is high, and comparable even to nanoparticles produced by laser ablation.[8,9] However, compared to laser ablation the SDG has a much higher potential for up-scaling as it is a more energy efficent method. Furthermore, recent developments of a high voltage switched SDG unit has further increased the energy efficency.[10]

The SDG generates nanoparticles by electric ablation; the electrode material is locally vaporised and forms a supersaturated vapor, that condenses into singlet nanoparticles, which grow spherically by coalesence.[11,12] However, at a critical size the particles can no longer grow by coalesence, but proceed via agglomeration. Agglomerated particles are fractal structures that consist of similarly sized primary particles.[13] Therefore, in order to produce larger spherical particles, it is necessary to compact the agglomerates, for example with thermal compaction.

Thermal compaction has been proposed to occur by an increase in surface or grain boundary diffusion,[14] and a temperature (in Kelvin) in the range of $\frac{1}{3} - \frac{2}{3}$ of the bulk melting temperature is often sufficent for full compaction.[15] At higher temperatures: new crystal structures and facets form,[16] and the particles may evaporate or be thermally charged.[17] Oxides are known to be more difficult to compact thermally, because of higher melting point, decreased diffusion,[15] and increased activation energy for reconstruction.[14] By introducing a reducing H_2 atmosphere during compaction the activation energy can be reduced, which enables compaction at lower temperatures. However, the immediate benefits and disadvantages of using a reducing atmosphere supplied at the particle generation has to our knowledge not been

Table 1: List of electrodes used to generate nano-particles.

Material	Purity [%]	Melting point [°C]
Cobalt	99.99	1495
Gold	99.95	1064
Bismuth	99.999	272

studied before. We show that 5% hydrogen is sufficient to result in a significant difference in compaction for both Co and Bi agglomerates. The thermal compaction is estimated by measuring the electrical mobility before and after compaction, as well as comparing morphology with transmission electron microscopy (TEM).

2   Method

Particle generation set-up   Nanoparticles of Co, Au and Bi were generated using a SDG (figure 1 from electrodes listed in table 1.
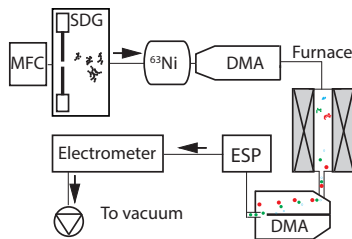

Figure 1: The spark discharge generator produces particles in a carrier gas, the particles are neutralised by a radioactive [63]Ni source, and size-selected in two differential mobility analyzers (DMAs) equipped in tandem, separated by a tube furnace. Finally an electrostatic precipitator (ESP) is used for particle deposition and an electrometer for particle concentration measurements.

Two different carrier gases were used and controlled by a mass flow controller (MFC), either 99.999 % N_2, referred to as pure nitrogen, or 95 % N_2 and 5 % H_2, referred to as hydrogen mixture. The carrier gas flow was set to 1.68 slm and the pressure of the system to 1004 kPa. Before initiating the experiments the system was pumped down to < 10 mbar and purged with nitrogen twice.

Particle generation was performed by spark discharge between two electrodes set 2 mm apart. The discharge frequency and energy was indirectly controlled by connecting the electrodes to a capacitance of 38 nF, charged with a current of 10 mA. The electrodes acts as a switch, which triggers a discharge when the bias over the capacitance exceeds the breakdown voltage of the electrode gap.[7] A radioactive [63]Ni foil was used to neutralize the particle charge distribution, forming mostly singly charged nanoparticles, required for electrical mobility classification.[18] Thereafter, two differential mobility analyzers (DMAs) were used to size-select particles before and after a compaction furnace. Finally the particle concentration was measured with an electrometer and a custom built electrostatic precipitator (ESP) for particle deposition.

Mobility diameter   The compaction of nanoparticles was measured with the tandem DMA set-up to measure negatively charged nanoparticles. Particles with a mobility diameter of 80 nm were selected with the first DMA (long TSI 3081) and transported through the Lenton tube furnace. The temperature of the furnace was adjusted with steps of 25 °C, up to 600 °C and the mobility size after compaction was measured by scanning the second DMA (a custom built Vienna type[19] and measuring the particle concentration with the TSI 3086B electrometer. When compacting above 600 °C the steps between temperatures varied. The measured particle distribution was fitted to a log-normal distribution, where the mean is used to describe the size of the compacted nanoparticles. The compaction temperature, defined as the temperature where no more shrinking of particle diameter occur, was identified and noted. At higher temperatures thermal charging was accounted for by comparing the particle distribution to the expected particle sizes for multiply charged particles.

TEM characterisation   Depositions of Au, Co and Bi nanoparticles were performed for both carrier gas compositions at selected temperatures. This was performed at a seperate date to verify the reproducibility of the previous compaction scans. First a compaction scan was performed and compared to previous results, thereafter the second DMA was bypassed and the 80 nm agglomerate nanoparticles were compacted and deposited on TEM Cu lacey-carbon grids with the ESP. High-resolution transmission electron microscopy (HRTEM) was performed with a 300 keV JEOL 3000F. Energy dispersive x-ray spectroscopy in

2

scanning transmission electron microscopy (STEM) mode was used to verify the composition of individual nanoparticles. The TEM samples were stored in a high purity nitrogen glovebox until the day of TEM analysis, in order to limit oxidation prior to analysis.

3 Results

The thermal compaction scans of the materials in table 1 are presented in figure 2. Each subpanel shows the compaction behaviour of one material for the two carrier gases, pure nitrogen and hydrogen mixture. For Au no clear difference is observed for the two gases, see figure 2 a). However, for Bi and Co there is a clear difference depending on carrier gas, see figure 2 b) and c). Furthermore, the particle distribution for Co generated in the hydrogen mixture compacted at 600 °C exhibited a clear bi-modal particle distribution, and the peak position of both are represented in figure 2 c). This bi-modal distribution was not observed at neither 575 °C or 625 °C.

3.1 Compaction - Mobility diameter

The repeated mobility scans performed before particle deposition were in good agreement with the thermal compaction scans presented in figure 2 (not presented).

Gold nanoparticles show the same compaction behaviour for the two gases. Compaction occurs gradually in the temperature range $20 - 375$ °C decreasing the particle size from 84 to 47 nm. The compaction temperature is determined to be 375 °C as the mobility diameter is constant in the observed interval $(375 - 675$ °C).

Bismuth nanoparticles show barely no compaction up to 300 °C, regardless of carrier gas type. The particles generated in the high purity nitrogen gas compact rapidly in the temperature range $325 - 450$ °C, where the particle size decreased from 78 to 44 nm. In the temperature range $450 - 600$ °C, the particles reach the compaction temperature and a particle size of 35 nm. Particles generated in the hydrogen mixture begins to compact at a lower temperature and has a lower compaction temperature, $\sim 250 - 400$ °C, compacting from $82 - 55$ nm particles. However, at $570 - 700$ °C the particles decrease in size again.

Cobalt nanoparticles show a similar weak compaction behavior up to 350 °C, regardless of gas type. Particles generated in the high purity nitrogen environment compact gradually in the entire observed temperature range, reaching a diameter of 50 nm when heated at 900 °C. In the range $350 - 600$ °C the mobility size diameter for particles generated in the hydrogen mixture is larger. However, at 600 °C a bi-modal particle distributions was identified, with a peak at 67 nm and one at 39 nm. Only the 39 nm peak was present at 625 °C to 800 °C. At 900 °C the particle size has decreased again, ~ 31 nm.
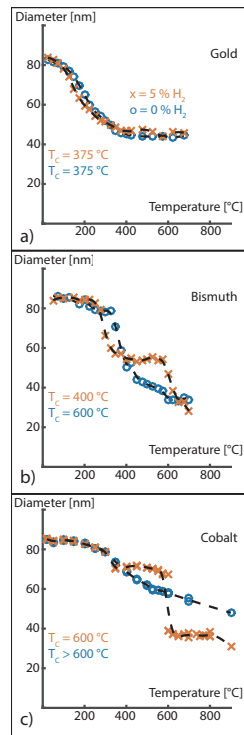

Figure 2: Mobility size diameter after compaction in a tube furnace for 80 nm agglomerate of different materials a) Au, b) Bi, c) Co. Particles are generated in two different gases, orange "x" represents 95 % N_2 and 5 % H_2, blue "o" represents 99.999 % N_2. Dashed lines are visual guidelines

3.2 Compaction - TEM

Depositions of typical nanoparticles generated with the two different gases and compacted at selected temperatures are presented by TEM images, see figure 3 for Au, figure 4 for Bi and figure 5 for Co. The subpanels are ordered so that the first column contains particles generated with the high purity N_2 and the the second column contains particles generated in the H_2 mixture. The composition of the presented nanoparticles was confirmed by energy dispersive x-ray spectroscopy to consist of the same material as the electrode material. However, eventual impurities were not successfully identified.

Figure 3 shows TEM of typical Au nanoparticles compacted at different temperatures. The images are in good agreement with the results from figure 2 a), and verifies that hydrogen has a negligible effect on the compaction behavior for 80 nm gold agglomerates. The agglomerate and primary particle size is similar for non-sintered particles ($\sim$ 5 nm, see 3 a) and b). The compacted particle size ($\sim$ 40 nm) and shape is comparable when compacted at 500 °C, see figure 3 c) and d).
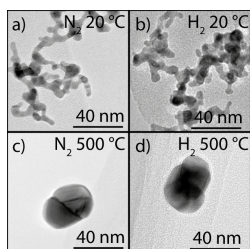

Figure 3: Au nanoparticles deposited at various temperatures for the two carrier gases, imaged by TEM

Figure 4 shows TEM of typical Bi nanoparticles compacted at different temperatures. As predicted from the mobility scans in figure 2 b) the particles are agglomerated for lower compaction temperatures, see figure 2 a) and b) for 20 °C and figure 2 c) and d) for 200 °C. At 300 °C, compaction is not perceivable for particles generated in pure nitrogen gas, see figure 2 e), but is almost complete for particles generated in a H_2 environment, see figure 2 f). Similar observations have been obtained at 400 °C for 60 nm agglomerates, see supplementary figure 6. The particles generated in the hydrogen mixture remain compact and similar in size

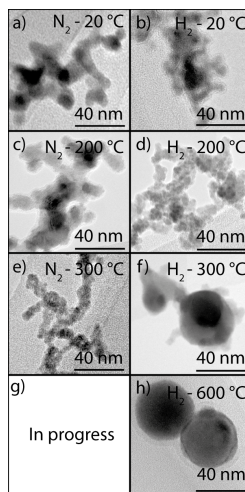up to 600 °C, see figure 4 h).

Figure 4: Bi nanoparticles deposited at various temperatures for the two carrier gases, imaged by TEM

Figure 5 shows TEM images of Co nanoparticles compacted at different temperatures. When generated in a hydrogen mixture and compacted at 600 °C, both agglomerated and compacted nanoparticles are present, see figure 5 b). At higher temperatures, d) 700 °C and f) 900 °C, only compacted nanoparticles were found. Co nanoparticles generated in a nitrogen flow and compacted in the range of $600 - 900$ °C do not compact into spherical nanoparticles, see figure 5 a), c) and e). Rather, with increasing temperature the agglomerate structure transforms to nanoparticles consisting of fewer larger faceted nanoparticles.

4 Discussion

When hydrogen is introduced in the carrier gas prior to particle generation only a miniscule fraction should reach the tube furnace where compaction proceeds. A DMA transfers particles from one gas flow to another, in this case from the hydrogen mixed carrier flow to the pure nitrogen sheath flow of the DMA. The flows are laminar, and mixing should be minimal and occur mainly by diffusion. Therefore, the H_2 concentration inside the tube furnace should be much lower than
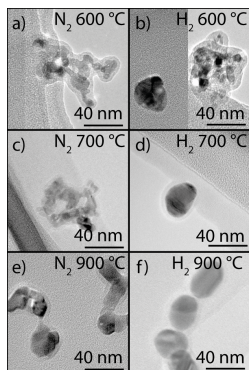
4

a) N$_2$ 600 °C b) H$_2$ 600 °C

40 nm 40 nm

c) N$_2$ 700 °C d) H$_2$ 700 °C

40 nm 40 nm

e) N$_2$ 900 °C f) H$_2$ 900 °C

40 nm 40 nm

Figure 5: Co nanoparticles deposited at various temperatures for the two carrier gases, imaged by TEM

upper limit of 0.7 % H$_2$ expected for complete mixing. We propose that hydrogen has an effect on the compaction temperature by hindering the formation of oxides at the stage of particle generation, thereby forming oxide free particles that are more easily compacted, due to the lower melting point and reduced surface impurities.[15]

Gold is a noble metal, and if the reduction in compaction temperature for Co and Bi nanoparticles is oxide related, no effect is expected for Au. This was verified with both mobility diameter scans and TEM analysis. Furthermore, it agrees well with previous research on SDG generated Ni and Pt nanoparticles, where hydrogen added during compaction decreased the compaction time for Ni but not for Pt nanoparticles.[20]

Bismuth nanoparticles were observed to compact into more spherical nanoparticles when generated in a hydrogen mixture. However, the compaction temperature was above the bulk melting point. We have two possible explanations for this, surface contaminations or the formation of a higher melting point compound. Surface contaminations are known to affect the kinetics of compaction,[14] and can thus be highly temperature sensitive. This is observed for Bi and Co near 300 °C and 600 °C, where the compaction behaviour deviates from the compaction of particles generated in pure nitrogen. We speculate that the high hydrogen concentration could form water by reacting with residual oxygen content in the system. The water might condense on the particles and evaporate during

the thermal compaction. However it is unclear why this would be beneficial for the thermal compaction. Another more plausible explanation is the formation of oxides such as Bi$_2$O$_3$ with a higher melting temperature of 817 °C, corresponding to a $\frac{T_C}{T_M}$ of 0.53. An oxide would compact at higher temperature, and if possible to thermally reduce would yield a shrinking particle size during the reduction. We speculate that the particles generated in hydrogen are protected from oxidation in the hydrogen mixture, but following the first DMA may partially oxidise, this would explain the higher than expected compaction temperature. The second decrease in size is also expected if bismuth begins to evaporate. Similarly, if the particles generated in nitrogen oxidised already at generation the particles may be more oxidised and the oxide effect on compaction stronger. This is supported by the higher compaction temperature and smaller final particle size for particles generated in the pure nitrogen flow.

Cobalt nanoparticles were observed to compact into more spherical nanoparticles when generated in hydrogen. However, in the range of $400 - 600$ nm they compacted less than the particles generated in high purity nitrogen. When generated in nitrogen the mobility diameter gradually decreased and the morphology changed, forming fewer but larger primary nanoparticles. In comparison to particles generated in hydrogen, where compaction occurred rapidly after reaching the critical compaction temperature of 600 °C, where both agglomerated and spherical particles were present. We speculate that surface contaminants (e.g water, oxides), might hinder compaction but be evaporated or reduced at high temperatures, resulting in a rapidly compacted nanoparticle. If the particles generated in nitrogen are fully oxidised this process would be much slower, leading to a gradual compaction.

The compaction temperature is an interesting observation, but is not an inherent property of a material. A literature study concerning Ag, Au, PbS, Fe, SnO$_2$, TiO$_2$ has reported that the compaction temperature often lies in the interval of $\frac{1}{3}$ to $\frac{2}{3}$ of the melting temperature (in Kelvin).[15] This is in agreement with our results for Au ($\frac{T_C}{T_M} = 0.50$), and Co ($\frac{T_C}{T_M} = 0.49$). However, compaction is a kinetic process, and depending on the initial agglomerate size[21] and particle purity[16] the compaction temperature can differ. Moreover, temperature gradients inside the tube furnace and the carrier flow will affect the compaction rate and time, resulting in an expected discrep-

5

ancy between experimental set-ups.

5 Conclusions

Adding hydrogen during generation has shown to have clear benefits when generating non-noble metals and no effect for noble Au nanoparticles. Cobalt and bismuth, both showed undesired compaction characteristics when using a high purity nitrogen carrier gas. Cobalt gradually decreased in mobility diameter and the primary particle size grew, forming anisotropic particles with faceted primary particles. When adding hydrogen, a clear compaction temperature was observed at 600 °C, resulting in the formation of spherical particles. Bismuth nanoparticles required temperatures exceeding the melting point to compact fully for both the pure nitrogen and the reducing hydrogen atmosphere. However, when generated in hydrogen the particles compacted at lower temperatures and formed more spherical nanoparticles.

We have argued that the hydrogen improves the particle purity during formation, and speculated how as a side product water may form. Further research will be required to convincingly support the mechanism and extent of the observed effects. However, the work has definitely showed that adding hydrogen during generation is clearly beneficial for the size control of the produced metal nanoparticles, and we see no obstacles for this to be incorporated in other aerosol production methods.

6 Acknowledgments

References

[1] M. H. Magnusson, B. J. Ohlsson, M. T. Björk, K. A. Dick, N. T. Borgström, K. Deppert, and L. Samuelson. Semiconductor nanostructures enabled by aerosol technology. *Frontiers of Physics*, 9(3):398–418, jan 2014.

[2] S. L. Suib, H. Ramsurn, and R. B. Gupta. *New and Future Developments in Catalysis*. Elsevier, 2013.

[3] A. Kumar Gupta and M. Gupta. Synthesis and surface engineering of iron oxide nanoparticles for biomedical applications. *Biomaterials*, 26:3995–4021, 2005.

[4] K. Fan, C. Cao, Y. Pan, D. Lu, D. Yang, J. Feng, and L. Song. Magnetoferritin nanoparticles for targeting and visualizing tumour tissues. *Nature Nanotechnology*, 7(July), 2012.

[5] V. A. Vons, L. C. P. M. Smet, D. Munao, A. Evirgen, E. M. Kelder, and A. Schmidt-Ott. Silicon nanoparticles produced by spark discharge. *Journal of Nanoparticle Research*, 13(10):4867–4879, jun 2011.

[6] A. Schmidt-ott and T. V. Pfeiffer. WO2013115644A11.pdf, 2013.

[7] B. O. Meuller, M. E. Messing, D. L. J. Engberg, A. M. Jansson, L. I. M. Johansson, S. M. Norlén, N. Tureson, and K. Deppert. Review of Spark Discharge Generators for Production of Nanoparticle Aerosols. *Aerosol Science and Technology*, 46(11):1256–1270, nov 2012.

[8] J F Ready. Development of plume of material vaporized by giant pulse laser. *Applied Physics Letters*, 3(11):11–13, 1963.

[9] T. E. Itina and A. Voloshko. Nanoparticle formation by laser ablation in air and by spark discharges at atmospheric pressure. *Applied Physics B*, 113:473–478, 2013.

[10] T.V. Pfeiffer, J. Feng, and a. Schmidt-Ott. New developments in spark production of nanoparticles. *Advanced Powder Technology*, 25(1):56–70, jan 2014.

[11] J. Feng, G. Biskos, and A. Schmidt-Ott. Toward industrial scale synthesis of ultrapure singlet nanoparticles with controllable sizes in a continuous gas-phase process. *Scientific Reports*, 5(February):15788, 2015.

[12] J. Feng, L. Huang, L. Ludvigsson, M. E. Messing, A. Maisser, G. Biskos, and A. Schmidt-Ott. General Approach to the Evolution of Singlet Nanoparticles from a Rapidly Quenched Point Source. *The Journal of Physical Chemistry C*, 120(1):621–630, 2016.

[13] F. E. Kruis, K. A. Kusters, S. E. Pratsinis, and B. Scarlett. A Simple Model for the Evolution of the Characteristics of Aggregate Particles Undergo-

6

ing Coagulation and Sintering. *Aerosol Science and Technology*, 19(4):514–526, 1993.

[14] A. P. Weber and S. K. Friedlander. In situ determination of the activation energy for restructuring of nanometer aerosol agglomerates. *Journal of Aerosol Science*, 28(2):179–192, 1997.

[15] M. N. A. Karlsson, K. Deppert, L. S. Karlsson, M. H. Magnusson, J. O. Malm, and N. S. Srinivasan. Compaction of agglomerates of aerosol nanoparticles: A compilation of experimental data. *Journal of Nanoparticle Research*, 7(1):43–49, 2005.

[16] A. Schmidt-Ott. New approaches to in situ characterization of ultrafine agglomerates. *Journal of Aerosol Science*, 19(5):553–563, 1988.

[17] M. H. Magnusson, K. Deppert, J. Malm, J. Jan-Olov Bovin, and L. Samuelson. Gold nanoparticles: Production, reshaping, and thermal charging. *Journal of Nanoparticle Research*, 1:243–251, 1999.

[18] B. Y. H. Liu and D. Y. H. Pui. Electrical neutralization of aerosols. *Journal of Aerosol Science*, 5(5):465–472, 1974.

[19] E. O. Knutson and K. T. Whitby. Aerosol classification by electric mobility: apparatus, theory, and applications. *Journal of Aerosol Science*, 6(6):443–451, 1975.

[20] M. Seipenbusch, A. P. Weber, A. Schiel, and G. Kasper. Influence of the gas atmosphere on restructuring and sintering kinetics of nickel and platinum aerosol nanoparticle agglomerates. *Journal of Aerosol Science*, 34(12):1699–1709, 2003.

[21] K. Nakaso, M. Shimada, K. Okuyama, and K. Deppert. Evaluation of the change in the morphology of gold nanoparticles during sintering. *Journal of Aerosol Science*, 33(7):1061–1074, 2002.
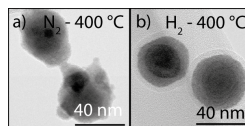
Figure 6: TEM of 60 nm Bi agglomerates after compaction at 400 °C. Particles generated in a hydrogen mixture are more compact than particles generated in a nitrogen mixture.

7 Supplementary Information

Paper 11

INVITED FEATURE PAPER

Palladium seeded GaAs nanowires

Robert T. Hallberg[a)] and Sebastian Lehmann
Solid State Physics, Lund University, 221 00 Lund, Sweden

Maria E. Messing
Solid State Physics, Lund University, 221 00 Lund, Sweden; and Synchrotron Radiation Research, Lund University, 211 00, Lund, Sweden

Kimberly A. Dick
Solid State Physics, Lund University, 221 00 Lund, Sweden; and Centre for Analysis and Synthesis, Lund University, 221 00 Lund, Sweden

In this work, we present a detailed investigation of the growth of palladium-seeded GaAs nanowires. Nanowires grown on GaAs (111)B substrates consist of three different morphologies, denoted as curly (containing multiple kinks), inclined (relative to the substrate, such as $\langle 001 \rangle$), and vertical. We show that the relative yield of the different types is controllable by a combination of V/III ratio and temperature, where vertical and inclined nanowires are promoted by a high temperature and low V/III ratio. These growth conditions are expected to promote a higher Ga incorporation into the Pd particle, which is confirmed by energy dispersive x-ray analysis. We propose that the observed relationship between particle composition and nanowire morphology may be related to the particle phase, with liquid particles promoting straight nanowire growth. In addition, particles at the tips of nanowires are sometimes observed to be smaller than the initial particle size, suggesting that Pd has been lost during the growth process. Finally, we demonstrate the importance of initial particle size-control to interpret diameter changes after growth.

I. INTRODUCTION

Gold nanoparticles are extensively used for seeding growth of III–V semiconductor nanowires, as they are known to yield uniform nanowire morphology over a large range of process conditions.[1] However, gold is well known to have a high diffusivity in silicon and to deteriorate its electrical properties by introducing mid-gap states,[2] complicating integration of III–V nanowires into Si-based devices. In addition, the most favorable growth direction for gold-seeded III–V nanowires is $\langle 111 \rangle$ B, while the $\langle 001 \rangle$ direction would be preferable for integration with Si electronics. Finally, gold-seeded nanowires grown in the $\langle 111 \rangle$ B direction have a strong tendency to form stacking faults,[3] which are also detrimental to the electronic properties.[4,5] For these reasons it is of great interest to explore gold-free growth techniques, for example using alternative metal seed particles. Pd and Fe have for example been shown to initiate the growth of nanowires in other preferential directions, including $\langle 110 \rangle$,[6,7] $\langle 111 \rangle$ A,[8,9] and $\langle 001 \rangle$,[7] in some cases without any stacking faults. In addition to defect-free zinc blende, more exotic polytypes, such as 4H, have been observed for example in Cu-seeded

nanowires.[10] Finally, intentional incorporation of atoms from the seed particle can potentially be used to tailor nanowire properties; for example Sn atoms from the seed particle have been used for doping,[11] and the incorporation of Fe or Mn is proposed to enable nanowires with magnetic properties.[7,12,13] Additional investigations include III–V nanowires grown using Ag,[14] Bi,[15] Nb,[16] Ni,[17] Ta,[18] and Tb[19] as seed particles. However, there is a lack of large-scale systematic growth parameter studies to understand the growth behavior of III–V nanowires seeded by particles of other materials than gold.

The steady-state phase of the seed nanoparticle during growth is an important consideration for the resulting nanowire properties. Depending on the particle phase, nanowire growth is governed by either the vapor–liquid–solid (VLS)[20] or the vapor–solid–solid (VSS)[21] mechanism. Gold-seeded growth typically occurs in the VLS regime (gold nanoparticles form liquid alloy droplets during nanowire growth), due to the low eutectic temperature of gold with many semiconductors. However, by alloying Au with Ag[22] or Al[23] a solid phase can be promoted (VSS growth), which has been shown to result in atomically sharp heterointerfaces for Si/Ge nanowires. VSS growth is typically associated with lower growth rates[24]; however in situ studies of Pd-seeded VSS growth of Si nanowires[25] show axial growth rates higher than typically reported for other VSS growth.[22] Further studies are needed to fully understand the effects of particle phase

and material on the resulting nanowire properties. Previous work on Pd-seeded InAs[6,8] and Cu-seeded InP[26] nanowire growth showed a coexistence of solid and liquid particles on a single growth substrate, suggesting that these materials are good candidates to directly compare the relationship between particle phase and nanowire properties.

In this work, we have studied Pd-seeded GaAs nanowires to gain further insight into the role of the particle during nanowire growth, enabling the transition to a variety of alternative seed materials with properties adapted to the desired nanowire properties and/or application. The Pd particles were generated as an aerosol using a spark discharge generator (SDG).[27] This technique allows for a high control of the initial particle density and size, making it possible to correlate postgrowth sizes and densities with the initial particle size and density. This is highly important, as particle diameter and proximity effects are known to influence both crystal structure and growth rate of the nanowires.[28,29] We show that Pd-seeded GaAs nanowires grow in various directions, including $\langle 111 \rangle$ and $\langle 001 \rangle$, depending on the growth conditions. Straight nanowires with a specific growth direction are promoted by a high growth temperature and low V/III ratio, in a region of the parameter space where nucleation and thus yield is low. In addition, energy dispersive x-ray spectroscopy (EDX) analysis shows that postgrowth seed particles contain a high amount of Ga if grown at high temperature and low V/III ratio. Although the initial Pd particle size was controlled, the postgrowth particle size varies and is often much smaller than the initial size, suggesting that Pd may be lost during growth.

II. METHOD

A. Nanowire growth

GaAs nanowire growth was carried out by metal–organic vapor phase epitaxy in an AIXTRON 3×2 in. close coupled showerhead (CCS) reactor (AIXTRON SE, Herzogenrath, Germany) at a pressure of 100 mbar and 8 slm of total gas flow with H_2 as the carrier gas. Before the actual nanowire growth, the aerosol decorated epi-ready GaAs (111)B substrates were annealed at a set temperature of 680 °C for 7 min under arsine (AsH_3) with a molar fraction 2.5×10^{-3} before setting the desired growth temperature. The parameter space for GaAs nanowire growth covered a set temperature range of 350–600 °C and a V/III ratio range from 0.4 to 65. The V/III ratio was changed by varying either trimethylgallium (TMGa) or AsH_3 with corresponding molar fractions between $\chi_{TMGa} = 6.98 \times 10^{-6} - 6.28 \times 10^{-5}$ and $\chi_{AsH_3} = 4.55 \times 10^{-5} - 2.25 \times 10^{-3}$ (the specific parameter changed is specified in the text). After growth, both sources were switched off and the samples were cooled under H_2.

Table I summarizes the growth parameters used for the temperature and V/III series presented in this paper. The two temperature series were performed at a V/III ratio of either 0.8 or 24 and the three V/III series were performed with set temperatures of either 450 or 580 °C. In the figures, a representative subset of samples is shown, whereas the complete series is available in the attached supplementary information.

To generate the palladium nanoparticles a SDG was used, see Figure S1. The particle distributions were adapted to the growth series after acquiring feedback from initial nanowire growth experiments. For the V/III series at 450 °C and temperature series at a V/III ratio of 24 the growth time was 5 min, and the substrates were decorated with 42 ± 3 nm Pd particles with a density of 11 μm^{-2}, see Fig. 1. For the temperature series at a V/III ratio of 0.8 and V/III series at 580 °C, the particle size was 40 ± 6 nm with a density of 1.5 μm^{-2}, we will refer to the initial diameter of both initial particle distributions to be 40 nm. Furthermore, a majority of the growth runs were performed on three GaAs (111)B substrates in parallel: one decorated with Pd aerosol particles, one decorated with Au aerosol particles of similar size and density, and finally one bare substrate.

B. Scanning electron microscopy (SEM) and transmission electron microscopy (TEM) characterization
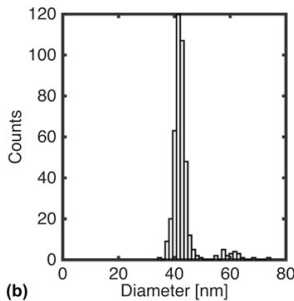
To evaluate the particle distribution before growth and to perform batch overview analysis of the growth, every nanowire sample was imaged using a Hitachi SU8010 SEM operated at an accelerating voltage of 15 kV (Hitachi, Tokyo, Japan). Size selection and density of the initial particle density was aided by the dedicated software nanoDim.[30] The resulting data were used to evaluate overall trends in nanowire morphology and to further carry out a statistical analysis of the relative yield of the different nanowire types (curly, inclined, and vertical; see Sec. IV. A for details). Images used for both initial particle and nanowire analysis were acquired at a 30° tilt angle at 2, 10, and 50 k magnification in the center of the sample with a high pixel density (2560 × 1920) to improve image analysis. For samples with observed local variations, additional images were acquired at different locations, often including an edge image. For estimating the yield of the different wires, an area corresponding to roughly 5000 μm^2 was investigated for each sample to count and measure the nanowires manually, whereof the number of vertical or inclined nanowires varied between 7 and 86 with an average of 42. To calculate the nanowire length of vertical nanowires, twice the projected length measured in 30° tilted SEM images was used. However, for inclined nanowires of unknown growth directions, the relationship between the measureable projected length and the true length is unknown. Similarly, curly nanowires kink repeatedly, resulting in the projected length, independent of

TABLE I. Temperatures and TMGa and AsH$_3$ molar fractions used for the different series presented in the manuscript.

Parameter varied (referred to as series)	Temperature (°C)	V/III	χ_{TMGa} (10^{-5})	χ_{AsH_3} (10^{-5})	Number of samples
Temperature	450–600	0.8	5.6	4.5	7
Temperature	350–600	24	3.1	75	7
V/III by AsH$_3$ variation	450	1.0–73	3.1	3.1–225	8
V/III by AsH$_3$ variation	580	0.4–1.6	5.6	2.3–8.8	4
V/III by TMGa variation	580	0.4–7.3	0.6–11.2	4.5	6
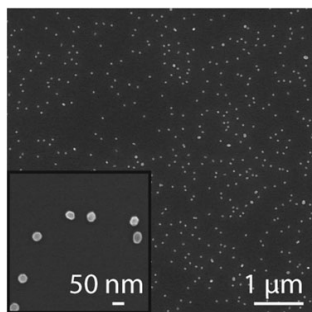
FIG. 1. (a) A top-view SEM image of the initial Pd particles before growth with a density of 11 μm^{-2}. In (b), the particle distribution from a bimodal fit yields a dominant peak centered at 42 nm ± 3 nm and a minor peak at 56 nm from overlapping particles.

imaging direction, which always is shorter than the true length. Therefore, the apparent growth rates of curly and inclined nanowires have only been compared qualitatively, side-by-side in SEM images.

Nanowire transfer for TEM analysis was performed by gently sliding a lacey carbon covered copper grid across the substrate. To ensure that representative nanowires from the entire sample were transferred onto the TEM grid, the mechanical transfer was applied to the entire substrate area. A 300 keV JEOL-3000F (JEOL Ltd., Tokyo, Japan) was used to investigate samples preselected by the SEM batch analysis. Nanowire crystal structure was investigated by high-resolution (HR)-TEM and selected area diffraction pattern (SADP) analysis. For compositional analysis of nanowires and postgrowth particles, EDX was carried out in scanning transmission electron microscopy or in conventional TEM bright field mode by converging the beam onto the nanoparticle, the EDX was aided by Oxford INCA software. The composition is represented in atomic % unless otherwise stated, with an estimated single measurement error of ±2 wt% absolute. Table II shows a mean of 4–10 different nanowires per sample and the error is represented by the sample standard deviation.

III. RESULTS

A. Morphology and structure

Nanowire growth was observed over a large parameter space with varying morphology; depending on growth conditions, one or several morphologies coexisted on the same substrate. To investigate the effect of growth parameters on morphology the nanowires were divided into three categories: curly, inclined, and vertical (Fig. 2). To observe differences in crystal structure, growth direction, and particle composition, TEM investigations were done on samples where the different types coexisted in reasonable fractions for statistical analysis.

Curly nanowires are defined by their frequently changing growth direction and numerous kinks. If grown for long enough the nanowires appear to swirl or curl, hence their name. See Fig. 2(a) for a SEM image of typical curly nanowires with clearly defined particles, where the width of the particle/nanowire interface varies across samples with an average of 57 ± 15 nm. The measurements were done in angles nonperpendicular to the nanowire/particle interface for 77 nanowires across 5 different samples, and this serves as a first approximation of the particle size on curly nanowires. Figure 2(b) shows a TEM bright field image of a curly nanowire. In Fig. 2(d), a typical faceted particle with a nonflat interface to the nanowire is observed. Note that the nonflat interface is not necessarily a consistent feature of the curly nanowires but has not been observed for the other

67

nanowire types. The SADP in Fig. 2(e) from the observed wire reveals a twinned zinc blende crystal structure. In addition, in Fig. 2(c), HRTEM of the structure shows two rotational twins, denoted as T_1 and T_2. Occasionally curly nanowires continue to grow along a single direction. TEM of such nanowires reveal a flat particle/nanowire interface, either inclined or perpendicular to the growth direction; see (Fig. SI 2).

Inclined nanowires are defined as nanowires that grow in a specific growth direction, inclined to the (111)B substrate, and have no more than one clearly visible kink. See Fig. 2(f) for a SEM image of inclined nanowires grown simultaneously with curly nanowires (visible in the background). Inclined nanowires are typically much longer than curly nanowires, interpreted as having a higher

TABLE II. Postgrowth gallium content of particles for different growth settings acquired by EDX. The values are presented as the mean Ga atomic % and the standard deviation of the distribution.

Temperature (°C)	V/III	Ga content (at.%)	Dominant wire types
450	0.8	40 ± 2	Curly
500	24	45 ± 2	Curly
580	0.8	67 ± 13[a]	Inclined > vertical
600	0.8	71 ± 6[a]	Vertical > inclined
580	1.2	47 ± 5[a]	Inclined
580	1.6	48 ± 3	Inclined

[a]Wide spread of compositions.

growth rate. In addition, these particular nanowires have four side-facets (only two of them visible in the SEM images), a barely visible particle at the tip, and are tapered. In Fig. 2(g), TEM image of a straight inclined nanowire from the same sample is shown, grown in a ⟨001⟩ growth direction with defect-free zinc blende crystal structure, as observed by zinc blende stacking in the high resolution inset [Fig. 2(h)] and SADP of the nanowire [Fig. 2(j)]. In Fig. 2 (i), the particle diameter is observed to be 25 nm, with a hemispherical or truncated spherical shape. Note that this is considerably smaller than the initial Pd particle diameter of 40 nm. EDX analysis shows that the particle consists of about 50% Ga and 50% Pd. Other growth directions are also expected from extensive SEM investigations, due to common orientations not consistent with ⟨001⟩ and the presence of nanowires with more than four facets; however, other specific orientations have not been confirmed.

Vertical nanowires are defined as nanowires that are growing straight and vertically aligned to the GaAs (111) B substrate and are thereby presumed to grow in a ⟨111⟩ B direction. See Fig. 2(k) for a SEM image of a vertical nanowire, which shows tapering and an apparently hexagonal cross section. This is similar to gold-seeded nanowires grown during the identical run; however, gold-seeded nanowires were observed to be shorter, see Fig. SI 3. In Fig. 2(l), a TEM bright field image of a straight nanowire from a sample with mostly vertical

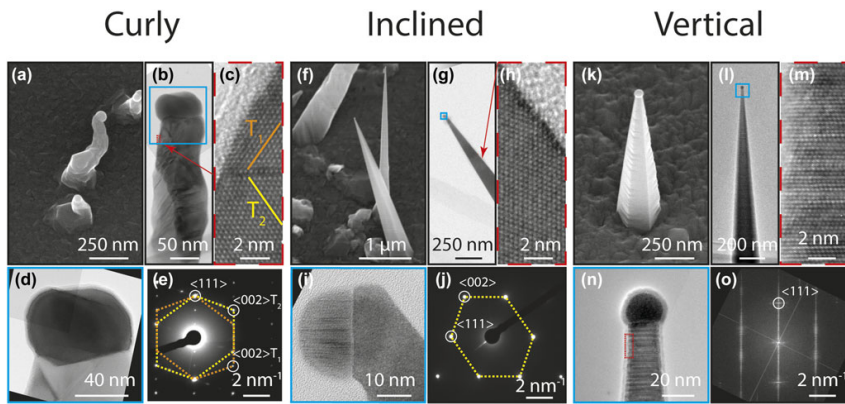## Curly   Inclined   Vertical

FIG. 2. (a) SEM image (30° tilt) of a typical curly nanowire grown at 500 °C and a V/III ratio of 24. (b) TEM image of a nanowire from the sample shown in (a), with a 75 nm wide particle and a nonflat particle/nanowire interface observed in (d). A twinned zinc blende crystal structure is observed from the inset in (c) and confirmed in the SADP of the wire in (e). (f) SEM image (30° tilt) of typical inclined nanowires grown at 580 °C and a V/III ratio of 1.2. (g) TEM image of a nanowire from the sample shown in (f), with a 25 nm particle/nanowire interface observed in (i). A defect-free zinc blende crystal structure and ⟨001⟩ growth direction are deduced from the SADP in (j) and the inset (h) from the wire in (g). (k) SEM image (30° tilt) of a typical vertical nanowire grown at 590 °C and a V/III ratio of 0.8. (l) TEM image of a vertical nanowire grown at 600 °C and a V/III ratio of 0.8, with a 22 nm truncated spherical particle observed in (n). A mixed crystal structure and a ⟨111⟩ growth direction are deduced from (m) and FFT of the wire in (o).

nanowires shows numerous rotational stacking defects and the fast Fourier transform (FFT) [Fig. 2(o)] confirms growth along a ⟨111⟩ direction. In Fig. 2(n), the particle is 22 nm in diameter and spherical (notably smaller than the initial Pd nanoparticle diameter of 40 nm). Additionally, EDX analysis of the particle shows a high Ga incorporation of 75%. Occasionally, vertical nanowires of varying length and particle size are also observed within the same sample, and the side facet smoothness varies (Fig. SI 4).

B. Effect of growth temperature

Investigation of the effect of temperature was performed for two V/III ratios; see Fig. 3 for a V/III ratio of 0.8, Fig. 4 for statistics on straight wires at this V/III ratio, and Fig. 5 for a V/III ratio of 24.
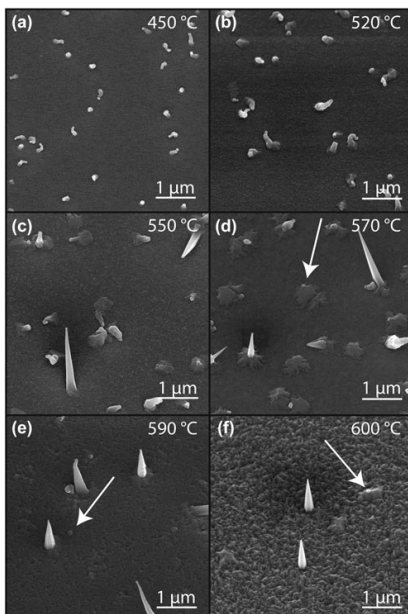

FIG. 3. Temperature series at a V/III ratio of 0.8, represented by 30° tilt SEM images. (a and b) Below 520 °C only curly nanowires are present. (c) At 550 °C, a mixture of nanowires is observed, including inclined nanowires. (d–f) The relative yield of vertical nanowires increases for increasing temperature and at 600 °C the majority of nanowires are vertical. In addition, the substrate surface is considerably rougher after growth at this temperature. Arrows indicate particles on the substrate (presumed to be Pd) that are not associated with a nanowire.

Figure 3 at a V/III ratio of 0.8 shows nanowires from a temperature series grown between 450 and 600 °C. At the lowest studied growth temperatures (450–520 °C) only curly nanowires are observed. At 550 °C inclined nanowires and occasional vertical nanowires are observed in addition to curly nanowires. However, compared to lower growth temperatures, especially to 450 °C, it is clear that the density of curly nanowires is lower. At 570–600 °C, very few curly nanowires are observed and most nanowires are either vertical or inclined. At the highest temperature investigated, 600 °C, we observe mostly vertical nanowires and a considerably rougher substrate surface. The total density of nanowires decreases with temperature, although the initial Pd nanoparticle density was identical for all samples shown here. Hence, not all particles form nanowires at higher temperatures, as is clearly observed from the particles visible on the substrate surface (with examples highlighted using arrows in Fig. 3).

Both vertical and inclined nanowires are observed throughout the temperature range of 550–600 °C, but the relative yield changes with growth temperature; see Fig. 4(a). There are more inclined nanowires than vertical for all but the highest temperature studied, 600 °C. Vertical nanowires are observed first at 550 °C, and the density increases for temperatures up to 590 °C and then decreases. Similarly, inclined nanowires are observed at 550 °C and the density increases for temperatures up to 570 °C and then decreases (inclined wires are occasionally
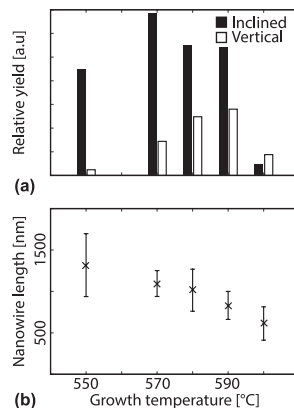

FIG. 4. (a) Yield of inclined and vertical nanowires normalised to the initial particle density for a V/III ratio of 0.8 and growth temperatures from 550 to 600 °C. This shows that the formation of vertical nanowires is promoted by a high growth temperature. (b) The mean length of vertical nanowires decreases with increasing temperature (error bars represent the standard deviation).
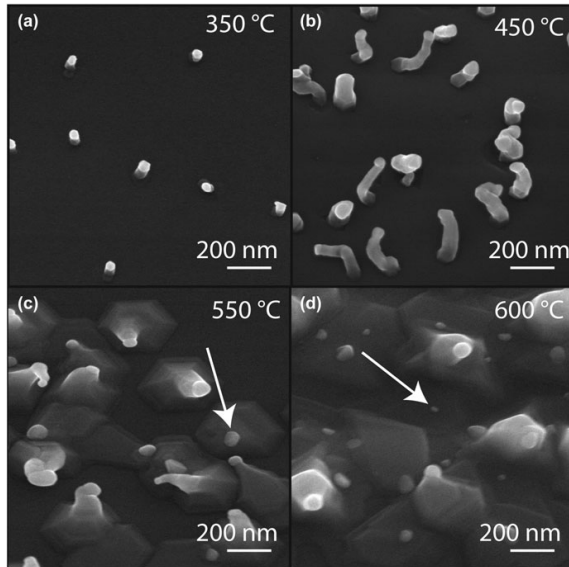
FIG. 5. Temperature series at a V/III ratio of 24, represented by 30° tilt SEM images. (a and b) Curly nanowires are observed at lower temperatures while (c and d) at higher temperatures fewer nanowires and substrate growth near the nanowire base are observed.

observed even at 520 °C) Furthermore, the average length of the vertical nanowires decreases with growth temperature [Fig. 4(b)], and varies considerably within the same sample.

Figure 5 shows SEM images of selected samples from a temperature series with a V/III ratio of 24; only selected temperatures that represent the major observations are shown. Note that for the 350 °C sample, a lower initial Pd particle density was used; however, density effects were observed to be negligible (see Fig. SI 5). For temperatures up to 400 °C, only very short nanowires are observed. Up to 500 °C, the typical curly nanowires described in connection with Fig. 2 are observed. However, at 550 °C and above, extensive substrate growth is apparent, especially at the nanowire base. In addition, occasional inclined nanowires similar to those grown at lower V/III ratios have been observed at 550 °C. Similarly, to the temperature series at a V/III ratio of 0.8 a decrease in nanowire density is observed at temperatures above 550 °C. The effect is best illustrated at the highest temperature, where higher contrast spots indicate Pd particles that have not initiated (nanowire) growth. Consequently, the main effect of temperature at this V/III

ratio is first an increase of growth rate, followed by a small region where inclined nanowires exist, and a transition to substrate/radial growth and reduced nanowire density. The full series is included in Fig. SI 6.

C. Effect of V/III ratio

Three V/III series were performed: two at 580 °C by varying either the AsH_3 (Fig. 6) or TMGa (Fig. 7) molar fraction and one at 450 °C (Fig. 8) by varying the AsH_3 molar fraction.

Figure 6 shows results from the V/III series performed by changing the AsH_3 supply at 580 °C. At a very low V/III ratio of 0.4, only short vertical nanowires are observed, while at a V/III ratio of 0.8, longer vertical nanowires and curly nanowires can be observed. At V/III ratios of 1.2 and 1.6, very long inclined nanowires can be recognized. In addition to the inclined nanowires, a larger number of shorter curly nanowires also exist on the substrate. An increase in growth rate with increasing AsH_3 is apparent from the increase in total volume of the nanowires, especially noticeable for straight nanowires. In comparison to the temperature series in Fig. 3, a similar morphology change from mixed nanowire types to
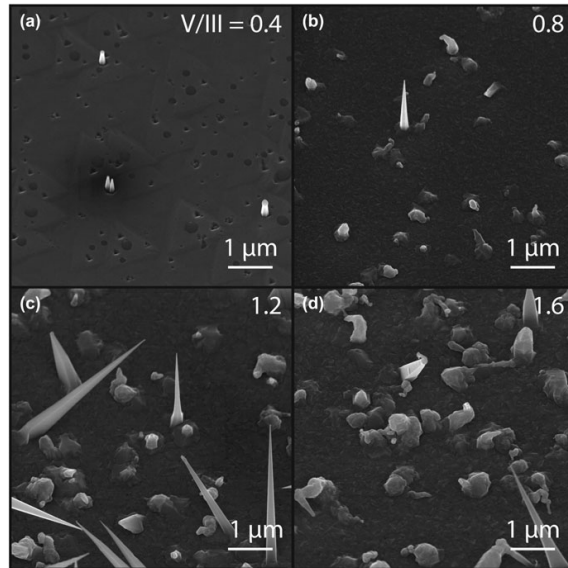
FIG. 6. V/III series at 580 °C by changing the AsH$_3$ supply, represented by 30° tilt SEM images. Increasing the V/III ratio controls the transition from (a) vertical, to (b) vertical and curly, to (c) inclined and curly, and (d) mostly curly with some inclined nanowires. In addition, a dramatic increase in nanowire length is observed.

mainly vertical nanowires is observed for decreasing V/III ratio (decreasing AsH$_3$ flow).

Figure 7 shows a V/III series performed by changing the TMGa supply at 580 °C. Similar to the AsH$_3$ series, a transition from vertical to mixed nanowire types is observed for increasing V/III ratio (decreasing TMGa flow). However, for this series, an increase of growth rate with increasing V/III ratio is not observed. This is perhaps reasonable since in the former case, we were increasing AsH$_3$, while here we decrease TMGa—indicating that the growth is As-limited. In addition, substrate growth near the base of the nanowires is substantial for V/III ratios above 2.4.

Figure 8 shows SEM images of selected samples from a V/III series performed by varying the AsH$_3$ supply at a growth temperature of 450 °C; selected samples are shown to represent the major observations. At V/III ratios below 1.8, only large particles compared to the initial Pd particle size are observed. For V/III ratios above 6.5, the nanowires are curly, and further increasing the AsH$_3$ flow causes no perceivable effect. This suggests that AsH$_3$ flow controls the growth rate at low growth temperatures and low V/III ratio (V-limited regime) but not at high

V/III ratio (III-limited regime). Note that for a V/III ratio of 6.5 a lower particle coverage of 1.5 μm^{-2} was used. Images of the complete V/III series are given in Fig. SI 7.

D. Particle analysis

Table II summarizes the EDX analysis of the post-growth particle composition depending on growth parameters and the dominant nanowire type of the sample. Only two samples show a very high Ga content, grown at a V/III ratio of 0.8 and temperatures of 580 and 600 °C. These are also the two samples with the highest proportions of vertical nanowires. However, the particle compositional analysis of nanowires grown at 580 °C and a V/III ratio of 0.8 shows a large standard deviation in Ga content strongly indicating that the composition of the particles varies. At lower temperatures and higher V/III ratios, the average Ga content was below 50% and the variation within each sample was lower. The vast majority of the particles showed an As content below the detection limit of the EDX analysis, however particles had up to 9% As, possibly originating from the nanowire.
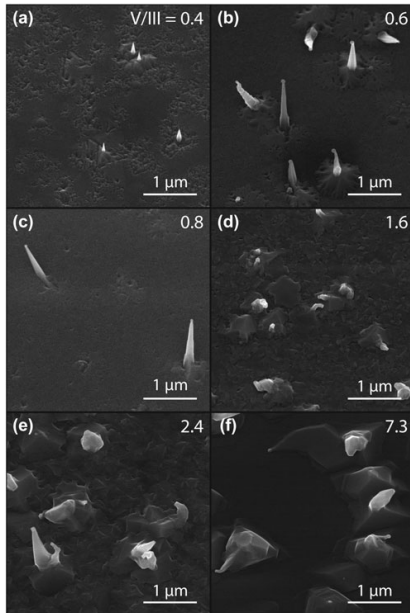
FIG. 7. V/III series at 580 °C by changing the TMGa supply, represented by 30° tilt SEM images. For a decreasing TMGa flow (increasing V/III ratio) a transition from (a–c) vertical to (d–f) curly nanowires can be observed.

To relate the postgrowth particle size to the known initial Pd nanoparticle size, a basic model was assumed to calculate the expected postgrowth size of a Pd–Ga alloy particle. We assumed a spherical particle and linear density dependence for x of Pd_xGa_{1-x}. The expected size increase with Ga incorporation is shown in Fig. 9, modeling the increase in size for 40 and 30 nm particles as a function of Ga incorporation. From the EDX measurements, we know that postgrowth particles typically consist of 40–50% Ga and in some extreme cases up to 80%. Assuming an initial particle size of 40 nm that would yield almost 50 nm particles for 50% Ga and 70 nm particles for 80% Ga. Such particles have been verified but, interestingly we have also observed particles far smaller than expected, such as the 22 nm particle with 75% Ga in Fig. 2(n), clearly not consistent with an initial particle size of 40 nm. This suggests that the nanoparticles may lose Pd either before or during the growth, for example via particle splitting or incorporation into the growing nanowire. Annealing tests were performed to

investigate if the annealing process caused any such effects, however, the results were difficult to interpret. To investigate possible incorporation of Pd into the nanowire, EDX spectra were acquired from several nanowires; however, the Pd signal was always below the detection limit of 2 wt.%. Making some geometric assumptions of truncated cylindrical nanowires, we calculate that the relative mass of the Pd nanoparticle is less than 0.2 wt.% for the two straight wires in Fig. 2. Thus, it is difficult to verify by EDX whether Pd has been incorporated.

IV. DISCUSSION

We have observed the formation of three different nanowire morphologies, denoted curly, inclined and vertical. From the explored process parameter space, we observe that high growth temperature and low V/III ratio suppress curly nanowires and promote straight nanowire growth. In parallel, we observe postgrowth a higher Ga content in the particle for nanowires grown at low V/III ratio and high growth temperature, and particles have a more spherical shape compared to the faceted particles observed at lower temperature and higher V/III ratio. From the Pd–Ga phase diagram,[31] it is known that the liquid phase is promoted by high Ga/Pd ratio and growth temperature. Furthermore, for growth conditions for which we observe both curly and straight nanowires, the straight nanowires are much longer, consistent with the faster growth rate often associated with VLS growth.[24,32] Therefore, we propose that the two straight nanowire types, inclined and vertical, are associated with liquid particles, while curly wires are associated with solid particles.

Curly nanowires have been observed to contain multiple rotational twinned zinc blende segments and sometimes to have a nonflat seed particle/nanowire interface. Nanowire growth from solid particles has previously been shown to occur by step/ledge-flow at the seed particle/nanowire interface[25,33]; thus, it has been proposed that such an anisotropic interface induces twin-mediated kinking, responsible for the curly morphology.[34] A solid Pd–Ga seed particle may therefore explain the observed curly morphology. Although VSS growth is generally associated with lower growth rates due to the lower bulk diffusion in solids than in liquids, the absolute magnitude of the growth rate also depends on the particle material. Solid Pd nanoparticles have previously been shown in-situ to seed Si nanowires at a remarkable rate, faster than nanowires grown with liquid gold seeds.[25] This is consistent with our observed curly wires, growing at rates similar to gold seeded nanowires.

Previous work for Pd-seeded InAs nanowires[34] reported a coexistence of curly nanowires with large particles and inclined nanowires with small particles. The
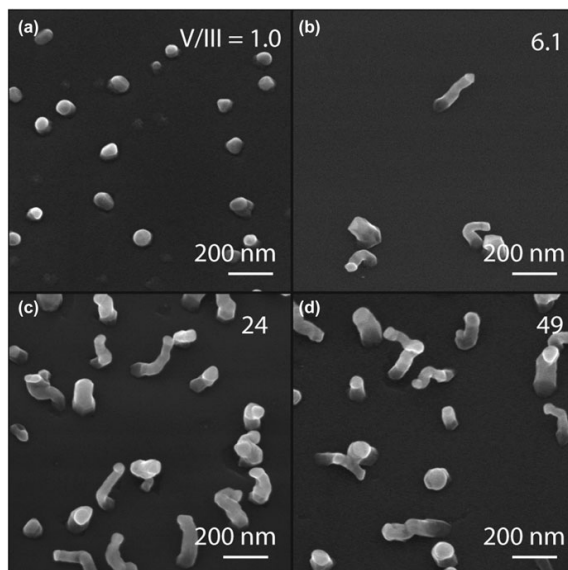
FIG. 8. V/III series at 450 °C by changing the AsH$_3$ supply, represented by 30° tilt SEM images. For an increasing AsH$_3$, (increasing V/III ratio) a transition from (a) low growth rate to (b–d) a higher growth rate is observed.
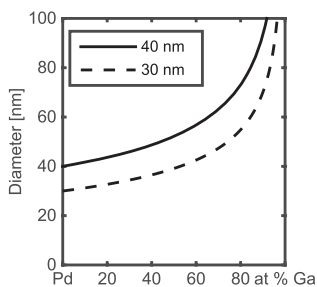

FIG. 9. Estimated diameter of palladium particles after Ga incorporation, for 40 and 30 nm initial particle diameters.

authors proposed that small particles were more likely to be liquid due to thermodynamic size effects, promoting growth of straight (inclined) nanowires, while larger particles remained solid and promoted curly nanowire growth. It is also well known that small particles promote growth directions such as ⟨112⟩ and ⟨110⟩.[35,36] However,

in this work, we have, for inclined and vertical Pd-seeded GaAs nanowires, observed particle sizes much smaller than what is expected from the initial particle size. Therefore, it appears that the small particles are not necessarily the cause of inclined and straight growth, but may be a side effect of, for example, unintentional incorporation of Pd into the nanowire. We speculate that the formation of liquid Pd–Ga droplets (rather than solid Pd–Ga particles) may lead to shrinking of the droplet due to a reduced detachment energy.

On the other hand, previous work also shows that the particle/substrate interface of a solid particle may control the nanowire growth direction, leading to for example Au-seeded ⟨001⟩ InAs[37] and Ni-seeded ⟨110⟩ Ge.[34] It may instead be that all of the nanowires in this study grow with solid particles, but that the different growth conditions and Ga contents lead to different favorable interfaces, in turn leading to the observed morphologies. Since the EDX analysis reported here is performed postgrowth, we cannot definitively conclude what the phase of the particle is during growth. Nevertheless, circumstantial evidence most strongly supports the hypothesis that straight nanowires grow from liquid

73

particles: These nanowires exhibit faster growth rates than curly nanowires (for the same growth conditions), more spherical particles postgrowth, and increased yield (relative to curly nanowires) under conditions for which liquid particles would be most likely to form.

For the explored parameter space, an increase in temperature yields fewer nanowires, attributed to nucleation difficulties. This is problematic for the use of Pd as a seed particle, since it is desirable to achieve nanowires with a high yield for specific growth directions. However, we note that both the inclined and (especially) vertical morphologies are most common for growth conditions where nucleation is difficult. For future applications it is of great interest to improve the nucleation, for example by using a two-step growth procedure,[38] starting at a different V/III ratio or temperature. However, we have only observed high nucleation rates for conditions leading to growth of only curly nanowires, which is highly unsuitable if a controlled growth direction is desired in the continued growth.

V. CONCLUSION

We have reported the growth of GaAs nanowires seeded from size- and density-controlled Pd nanoparticles at various growth temperatures and V/III ratios. The grown nanowires show three different types of morphologies, denoted as curly, inclined, and vertical. We show that in principle it is possible to tune between these with growth parameters, and among the straight morphologies confirm at least two different growth directions, $\langle 111 \rangle$ B and $\langle 001 \rangle$. We have shown that a low V/III ratio and high growth temperatures, conditions that by EDX are shown to promote a higher Ga incorporation into the Pd particles, in general promote straight nanowire growth. Differences observed in apparent growth rate, composition and the shape of the postgrowth particle suggest that only the straight nanowire types were grown with liquid particles, while curly nanowires most likely grow from solid particles. Furthermore, we have seen evidence that Pd may be lost during growth or annealing, as post growth particle sizes far smaller than the initial size have been observed. Our observations demonstrate that control of the seed nanoparticle phase and composition during growth may allow for selective tuning of nanowire growth direction and morphology.

ACKNOWLEDGMENTS

REFERENCES

1. K.A. Dick: A review of nanowire growth promoted by alloys and non-alloying elements with emphasis on Au-assisted III–V nanowires. *Prog. Cryst. Growth Charact. Mater.* **54**(3–4), 138–173 (2008).
2. A.J. Tavendale and S.J. Pearton: Deep level, quenched-in defects in silicon doped with gold, silver, iron, copper or nickel. *J. Phys. C: Solid State Phys.* **16**(9), 1665–1673 (1983).
3. J. Hornstra: Dislocations in the diamond lattice. *J. Phys. Chem. Solids* **5**(1–2), 129–141 (1958).
4. M.D. Schroer and J.R. Petta: Correlating the nanostructure and electronic properties of InAs nanowires. *Nano Lett.* **10**(5), 1618–1622 (2010).
5. C. Thelander, P. Caroff, S. Plissard, A.W. Dey, and K.A. Dick: Effects of crystal phase mixing on the electrical properties of InAs nanowires. *Nano Lett.* **11**(6), 2424–2429 (2011).
6. H. Xu, Y. Wang, Y. Guo, Z. Liao, and Q. Gao: Defect-free <110> zinc-blende structured InAs nanowires catalyzed by palladium. *Nano Lett.* **12**, 5744–5749 (2012).
7. I. Regolin, V. Khorenko, W. Prost, F.J. Tegude, D. Sudfeld, J. Kästner, G. Dumpich, K. Hitzbleck, and H. Wiggers: GaAs whiskers grown by metal-organic vapor-phase epitaxy using Fe nanoparticles. *J. Appl. Phys.* **101**(5), 1–5 (2007).
8. S. Heun, B. Radha, D. Ercolani, G.U. Kulkarni, F. Rossi, V. Grillo, G. Salviati, F. Beltram, and L. Sorba: Coexistence of vapor-liquid-solid and vapor-solid-solid growth modes in Pd-assisted InAs nanowires. *Small* **6**(17), 1935–1941 (2010).
9. S. Heun, B. Radha, D. Ercolani, G.U. Kulkarni, F. Rossi, V. Grillo, G. Salviati, F. Beltram, and L. Sorba: Pd-assisted growth of InAs nanowires. *Cryst. Growth Des.* **10**(9), 4197–4202 (2010).
10. K. Hillerich, D.S. Ghidini, K.A. Dick, K. Deppert, and J. Johansson: Cu particle seeded InP–InAs axial nanowire heterostructures. *Phys. Status Solidi RRL* **7**(10), 850–854 (2013).
11. R. Sun, D. Jacobsson, I-J. Chen, M. Nilsson, C. Thelander, S. Lehmann, and K.A. Dick: Sn-seeded GaAs nanowires as self-assembled radial p-n junctions. *Nano Lett.* **15**(6), 3757–3762 (2015).
12. F. Martelli, S. Rubini, M. Piccin, G. Bais, F. Jabeen, S. De Franceschi, V. Grillo, E. Carlino, F. D'Acapito, F. Boscherini, S. Cabrini, M. Lazzarino, L. Businaro, F. Romanato, and A. Franciosi: Manganese-induced growth of GaAs nanowires. *Nano Lett.* **6**(9), 2130–2134 (2006).
13. F. Jabeen, M. Piccin, L. Felisari, V. Grillo, G. Bais, S. Rubini, F. Martelli, F. D'Acapito, M. Rovezzi, and F. Boscherini: Mn-induced growth of InAs nanowires. *J. Vac. Sci. Technol., B* **28**(3), 478 (2010).
14. A.T. Vogel, J. de Boor, M. Becker, J.V. Wittemann, S.L. Mensah, P. Werner, and V. Schmidt: Ag-assisted CBE growth of ordered InSb nanowire arrays. *Nanotechnology* **22**(1), 015605 (2011).
15. D.D. Fanfair and B.A. Korgel: Bismuth nanocrystal-seeded III-V semiconductor nanowire synthesis. *Cryst. Growth Des.* **5**(5), 1971–1976 (2005).
16. H-Z. Zhuang, B.L. Li, C.S. Xue, X. Zhang, S.Y. Zhang, D-X. Wang, and J.B. Shen: Growth of Nb-catalysed GaN nanowires. *Microelectron. J.* **39**(12), 1629–1633 (2008).
17. X. Weng, R. Burke, and J. Redwing: The nature of catalyst particles and growth mechanisms of GaN nanowires grown by Ni-assisted metal–organic chemical vapor deposition. *Nanotechnology* **20**, 1–5 (2009).
18. H. Li, C. Xue, H. Zhuyang, J. Chen, Z. Yang, L. Qin, Y. Huang, and D. Zhang: Synthesis and characterization of GaN nanowires with Tantalum catalyst. *Mater. Chem. Phys.* **109**(2–3), 249–252 (2008).
19. J. Chen, C. Xue, H. Zhuang, L. Qin, H. Li, and Z. Yang: Synthesis of GaN nanowires by Tb catalysis. *Appl. Surf. Sci.* **254**(15), 4716–4719 (2008).

74

20. R.S. Wagner and W.C. Ellis: Vapor-liquid-solid mechanism of single crystal growth. *Appl. Phys. Lett.* **4**(5), 89–90 (1964).

21. A.I. Persson, M.W. Larsson, S. Stenström, B.J. Ohlsson, L. Samuelson, and L.R. Wallenberg: Solid-phase diffusion mechanism for GaAs nanowire growth. *Nat. Mater.* **3**(10), 677–681 (2004).

22. Y.C. Chou, C.Y. Wen, M.C. Reuter, D. Su, E.A. Stach, and F.M. Ross: Controlling the growth of Si/Ge nanowires and heterojunctions using silver-gold alloy catalysts. *ACS Nano* **6**(7), 6407–6415 (2012).

23. F.M. Ross, C-Y. Wen, S. Kodambaka, B.A. Wacaser, M.C. Reuter, and E.A. Stach: The growth and characterization of Si and Ge nanowires grown from reactive metal catalysts. *Philos. Mag.* **90**(20), 2807–2816 (2010).

24. S. Kodambaka, J. Tersoff, M.C. Reuter, and F.M. Ross: Germanium nanowire growth below the eutectic temperature. *Science* **316**(5825), 729–732 (2007).

25. S. Hofmann, R. Sharma, C.T. Wirth, F. Cervantes-Sodi, C. Ducati, T. Kasama, R.E. Dunin-Borkowski, J. Drucker, P. Bennett, and J. Robertson: Ledge-flow-controlled catalyst interface dynamics during Si nanowire growth. *Nat. Mater.* **7**(5), 372–375 (2008).

26. K. Hillerich, K.A. Dick, M.E. Messing, K. Deppert, and J. Johansson: Simultaneous growth mechanisms for Cu-seeded InP nanowires. *Nano Res.* **5**(5), 297–306 (2012).

27. B.O. Meuller, M.E. Messing, D.L.J. Engberg, A.M. Jansson, L.I.M. Johansson, S.M. Norlén, N. Tureson, and K. Deppert: Review of spark discharge generators for production of nanoparticle aerosols. *Aerosol Sci. Technol.* **46**(11), 1256–1270 (2012).

28. J. Johansson, K.A. Dick, P. Caroff, M.E. Messing, J. Bolinsson, K. Deppert, and L. Samuelson: Diameter dependence of the wurtzite-zinc blende transition in InAs nanowires. *J. Phys. Chem. C* **114**(9), 3837–3842 (2010).

29. B.M. Borg, J. Johansson, K. Storm, and K. Deppert: Geometric model for metalorganic vapour phase epitaxy of dense nanowire arrays. *J. Cryst. Growth* **366**, 15–19 (2013).

30. K. Storm: *NanoDim Software*. http://nanodim.kristian.storm.com (accessed December 03 2015).

31. B. Predel: Ga-Pd (Gallium-Palladium). *In Landolt-Börnstein – Group IV Physical Chemistry, Ga-Gd – Hf-Zr*, O. Madelung, ed. (Springer-Verlag: Berlin, 1996); pp. 57–59.

32. S.V. Thombare, A.F. Marshall, and P.C. McIntyre: Size effects in vapor-solid-solid Ge nanowire growth with a Ni-based catalyst. *J. Appl. Phys.* **112**(054325), 0–6 (2012).

33. C-Y. Wen, J. Tersoff, M.C. Reuter, E.A. Stach, and F.M. Ross: Step-flow kinetics in nanowire growth. *Phys. Rev. Lett.* **105**(19), 1–4 (2010).

34. H. Xu, Y. Guo, Z. Liao, and W. Sun: Catalyst size dependent growth of Pd-catalyzed one-dimensional InAs nanostructures. *Appl. Phys. Lett.* **102**, 203108 (2013).

35. V. Schmidt: Diameter-dependent growth direction of epitaxial silicon nanowires. *Nano Lett.* **5**(5), 931–935 (2005).

36. R.G. Cai, Y. Gong, and B. Wang: The size-dependent growth direction of ZnSe nanowires. *Adv. Mater.* **18**, 109–114 (2006).

37. Z. Zhang, K. Zheng, Z-Y. Lu, P-P. Chen, W. Lu, and J. Zou: Catalyst orientation-induced growth of defect-free zinc-blende structured ⟨00$\bar{1}$⟩ InAs nanowires. *Nano Lett.* **15**, 876–882 (2015).

38. H.J. Joyce, Q. Gao, H.H. Tan, C. Jagadish, Y. Kim, X. Zhang, Y. Guo, and J. Zou: Twin-free uniform epitaxial GaAs nanowires grown by a two-temperature process. *Nano Lett.* **7**(4), 921–926 (2007).

Supplementary Material

To view supplementary material for this article, please visit http://dx.doi.org/jmr.2015.400.

CAMBRIDGE JOURNALS

J. Mater. Res., Vol. 31, No. 2, Jan 28, 2016

185

75